

## Formation and evolution of carbonaceous asteroid Ryugu

### Direct evidence from returned samples

Nakamura, T.; Matsumoto, M.; Amano, K.; Enokido, Y.; Zolensky, M. E.; Mikouchi, T.; Genda, H.; Zolotov, M. Y.; Potin, S. M.; More Authors

**DOI**

[10.1126/science.abn8671](https://doi.org/10.1126/science.abn8671)

**Publication date**

2023

**Document Version**

Final published version

**Published in**

Science (New York, N.Y.)

**Citation (APA)**

Nakamura, T., Matsumoto, M., Amano, K., Enokido, Y., Zolensky, M. E., Mikouchi, T., Genda, H., Zolotov, M. Y., Potin, S. M., & More Authors (2023). Formation and evolution of carbonaceous asteroid Ryugu: Direct evidence from returned samples. *Science (New York, N.Y.)*, 379(6634), Article eabn8671. <https://doi.org/10.1126/science.abn8671>

**Important note**

To cite this publication, please use the final published version (if applicable). Please check the document version above.

**Copyright**

Other than for strictly personal use, it is not permitted to download, forward or distribute the text or part of it, without the consent of the author(s) and/or copyright holder(s), unless the work is under an open content license such as Creative Commons.

**Takedown policy**

Please contact us and provide details if you believe this document breaches copyrights. We will remove access to the work immediately and investigate your claim.

## RESEARCH ARTICLE SUMMARY

## COSMOCHEMISTRY

## Formation and evolution of carbonaceous asteroid Ryugu: Direct evidence from returned samples

T. Nakamura\* *et al.*

**INTRODUCTION:** Observations of asteroid Ryugu by the Hayabusa2 spacecraft found that it is a rubble pile, formed from fragments of a parent asteroid. Samples retrieved from Ryugu by the spacecraft were expected to contain a record of this history, including the formation and early evolution of the parent body, the subsequent impact destruction and partial reaccrction, and later space weathering. The composition of Ryugu was expected to be similar to that of Ivuna-type carbonaceous chondrite meteorites (CI chondrites).

**RATIONALE:** We investigated the formation history of Ryugu through laboratory analysis of the samples. Specifically, we sought to determine (i) when and where in the Solar System the parent asteroid formed; (ii) the original mineralogy, elemental abundances as a whole, and chemical compositions of the accreted materials, including their ice content; (iii)

how these materials evolved through chemical reactions; and (iv) how the material was ejected from the parent body in an impact. To address these issues, we analyzed 17 Ryugu particles of 1 to ~8 mm in size.

**RESULTS:** We found carbon dioxide (CO<sub>2</sub>)-bearing water in an iron-nickel (Fe–Ni) sulfide crystal, indicating that the parent body formed in the outer Solar System. Remanent magnetization was detected, implying that the solar nebula might still have been present when magnetite crystals formed on the parent body.

We used muon analysis to determine the abundances of light elements, including carbon (C), nitrogen (N), sodium (Na), and magnesium (Mg), whose abundances relative to silicon (Si) are similar to those in CI chondrites, whereas oxygen (O) is deficient compared with that in CI chondrites. X-ray computed tomog-

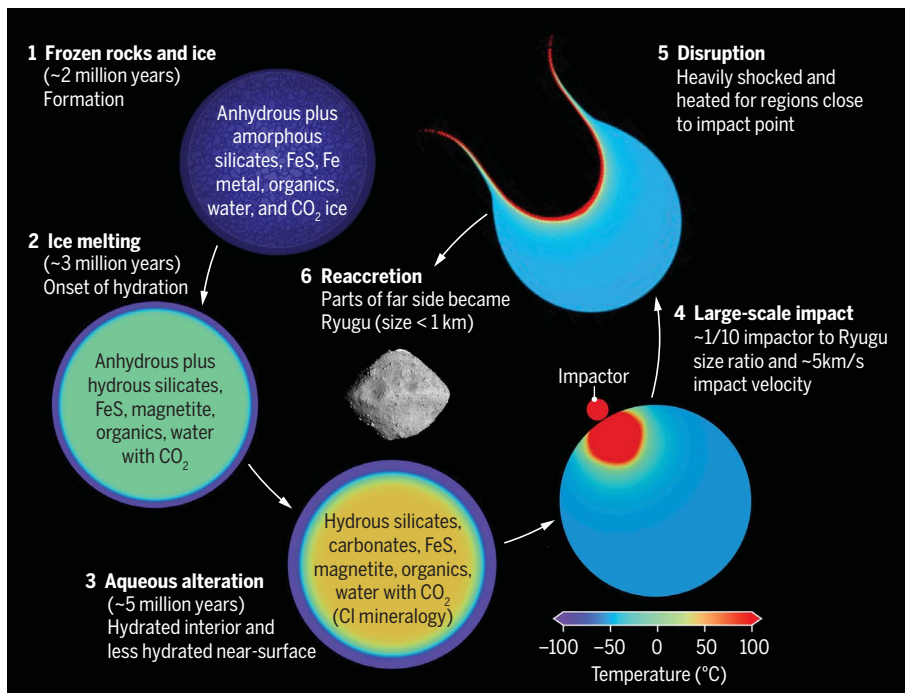
raphy analysis shows that all our Ryugu samples consist of fine-grained material. There are only rare objects of high-temperature origin, such as melted silicate-rich particles, all being smaller than 100 μm.

Electron microscope observations showed that the samples are breccias, assemblies of numerous small rock fragments with different compositions, mineralogies, and histories. The most common mineralogy contains Mg-rich hydrous silicates, MgCa and MgFe carbonates, hydroxyapatite, Fe sulfides, and Fe oxides. The mineralogy of this major lithology is consistent with classification as a CI chondrite. It also indicates widespread aqueous alteration (reactions with liquid water) on the parent body.

Some Ryugu fragments have a different mineralogy, containing anhydrous silicates (olivine and pyroxene), amorphous silicates, Ca carbonate, phosphides, Fe–Ni sulfide, Fe oxide, and poorly crystalline phyllosilicates. Some small objects (<~30 μm) that formed at high temperatures were also found. This mineralogy suggests that these fragments experienced less aqueous alteration.

We measured mechanical and thermal properties from the Ryugu samples. We found that they are similar, but not identical, to hydrated CI chondrites. Numerical simulations of the thermal history and impact disruption processes of the Ryugu parent asteroid were performed by incorporating the physical and mineralogical properties and appropriate water/rock ratios.

**CONCLUSION:** We propose that Ryugu's parent asteroid formed ~1.8 million to 2.9 million years after the beginning of Solar System formation, in the outer Solar System, where water and CO<sub>2</sub> were present as ice. It acquired a water ice/rock mass ratio in the range of 0.2 to 0.9. In this region, material formed at low temperatures is dominant, whereas material of high temperature origin is rare. In the interior of the parent asteroid, radioactive heating caused the water ice to melt at ~3 million years; water-rock reactions then gradually changed the initial anhydrous mineralogy to a largely hydrous mineralogy. At shallow depths, the original material was less altered, at a low water/rock ratio of <0.2. At ~5 million years, all material in the parent asteroid experienced its peak temperature, and aqueous alteration continued. An impact occurred ~1 billion years ago, disrupting the parent asteroid. Some fragments, originating away from the impact point, then reassembled to form Ryugu. ■



**Proposed model of Ryugu's formation history.** (1) A parent body asteroid forms in the outer Solar System, containing abundant ice. (2 and 3) Radioactive heating causes the ice to melt, which modifies the mineralogy through aqueous alteration reactions. (4 and 5) An impact then disrupts the parent body but does not cause widespread heating. (6) Ryugu formed from reaccumulation of ejected material that originated away from the impact point. All times were measured from the start of Solar System formation. Colors indicate estimated temperatures from our thermal interior and impact models.

The complete list of authors and their affiliations is available in the full article online.

\*Corresponding author. Email: tomoki.nakamura.a8@tohoku.ac.jp  
Cite this article as T. Nakamura *et al.*, *Science* 379, eabn8671 (2023). DOI: 10.1126/science.abn8671

**S READ THE FULL ARTICLE AT**  
<https://doi.org/10.1126/science.abn8671>

## RESEARCH ARTICLE

## COSMOCHEMISTRY

## Formation and evolution of carbonaceous asteroid Ryugu: Direct evidence from returned samples

T. Nakamura<sup>1\*</sup>, M. Matsumoto<sup>1</sup>, K. Amano<sup>1</sup>, Y. Enokido<sup>1</sup>, M. E. Zolensky<sup>2</sup>, T. Mikouchi<sup>3</sup>, H. Genda<sup>4</sup>, S. Tanaka<sup>5,6</sup>, M. Y. Zolotov<sup>7</sup>, K. Kurosawa<sup>8</sup>, S. Wakita<sup>9</sup>, R. Hyodo<sup>5</sup>, H. Nagano<sup>10</sup>, D. Nakashima<sup>1</sup>, Y. Takahashi<sup>11,12</sup>, Y. Fujioka<sup>1</sup>, M. Kikuir<sup>1</sup>, E. Kagawa<sup>1</sup>, M. Matsuoka<sup>13,14</sup>, A. J. Brearley<sup>15</sup>, A. Tsuchiyama<sup>16,17,18</sup>, M. Uesugi<sup>19</sup>, J. Matsuno<sup>16</sup>, Y. Kimura<sup>20</sup>, M. Sato<sup>11</sup>, R. E. Milliken<sup>21</sup>, E. Tatsumi<sup>22,11</sup>, S. Sugita<sup>11,8</sup>, T. Hiroi<sup>21</sup>, K. Kitazato<sup>23</sup>, D. Brownlee<sup>24</sup>, D. J. Joswiak<sup>24</sup>, M. Takahashi<sup>1</sup>, K. Ninomiya<sup>25</sup>, T. Takahashi<sup>26,27</sup>, T. Osawa<sup>28</sup>, K. Terada<sup>29</sup>, F. E. Brenker<sup>30</sup>, B. J. Tkalcic<sup>30</sup>, L. Vincze<sup>31</sup>, R. Brunetto<sup>32</sup>, A. Aléon-Toppini<sup>32</sup>, Q. H. S. Chan<sup>33</sup>, M. Roskosz<sup>34</sup>, J.-C. Viennet<sup>34</sup>, P. Beck<sup>35</sup>, E. E. Alp<sup>36</sup>, T. Michikami<sup>37</sup>, Y. Nagaashi<sup>38,1</sup>, T. Tsuji<sup>39,40</sup>, Y. Ino<sup>41,5</sup>, J. Martinez<sup>2</sup>, J. Han<sup>42</sup>, A. Dolocan<sup>43</sup>, R. J. Bodnar<sup>44</sup>, M. Tanaka<sup>45</sup>, H. Yoshida<sup>11</sup>, K. Sugiyama<sup>46</sup>, A. J. King<sup>47</sup>, K. Fukushi<sup>48</sup>, H. Suga<sup>49</sup>, S. Yamashita<sup>50,51</sup>, T. Kawai<sup>11</sup>, K. Inoue<sup>48</sup>, A. Nakato<sup>5</sup>, T. Noguchi<sup>52,53</sup>, F. Vilas<sup>54</sup>, A. R. Hendrix<sup>54</sup>, C. Jaramillo-Correa<sup>55</sup>, D. L. Domingue<sup>54</sup>, G. Dominguez<sup>56</sup>, Z. Gainsforth<sup>57</sup>, C. Engrand<sup>58</sup>, J. Duprat<sup>34</sup>, S. S. Russell<sup>47</sup>, E. Bonato<sup>59</sup>, C. Ma<sup>60</sup>, T. Kawamoto<sup>61</sup>, T. Wada<sup>1</sup>, S. Watanabe<sup>5,26</sup>, R. Endo<sup>62</sup>, S. Enju<sup>63</sup>, L. Riu<sup>64</sup>, S. Rubino<sup>32</sup>, P. Tack<sup>31</sup>, S. Takeshita<sup>65</sup>, Y. Takeichi<sup>50,51,66</sup>, A. Takeuchi<sup>19</sup>, A. Takigawa<sup>11</sup>, D. Takir<sup>2</sup>, T. Tanigaki<sup>67</sup>, A. Taniguchi<sup>68</sup>, K. Tsukamoto<sup>1</sup>, T. Yagi<sup>69</sup>, S. Yamada<sup>70</sup>, K. Yamamoto<sup>71</sup>, Y. Yamashita<sup>69</sup>, M. Yasutake<sup>19</sup>, K. Uesugi<sup>19</sup>, I. Umegaki<sup>72,65</sup>, I. Chiu<sup>25</sup>, T. Ishizaki<sup>5</sup>, S. Okumura<sup>52</sup>, E. Palomba<sup>73</sup>, C. Pilorget<sup>32,74</sup>, S. M. Potin<sup>13,75</sup>, A. Alasli<sup>10</sup>, S. Anada<sup>71</sup>, Y. Araki<sup>76</sup>, N. Sakatani<sup>70,5</sup>, C. Schultz<sup>21</sup>, O. Sekizawa<sup>49</sup>, S. D. Sitzman<sup>77</sup>, K. Sugiura<sup>4</sup>, M. Sun<sup>17,18,78</sup>, E. Dartois<sup>79</sup>, E. De Pauw<sup>31</sup>, Z. Dionnet<sup>32</sup>, Z. Djouadi<sup>32</sup>, G. Falkenberg<sup>80</sup>, R. Fujita<sup>10</sup>, T. Fukuma<sup>81</sup>, I. R. Gearba<sup>43</sup>, K. Hagiya<sup>82</sup>, M. Y. Hu<sup>36</sup>, T. Kato<sup>71</sup>, T. Kawamura<sup>83</sup>, M. Kimura<sup>50,51</sup>, M. K. Kubo<sup>84</sup>, F. Langenhorst<sup>85</sup>, C. Lantz<sup>32</sup>, B. Lavina<sup>86</sup>, M. Lindner<sup>30</sup>, J. Zhao<sup>36</sup>, B. Vekemans<sup>31</sup>, D. Baklouti<sup>32</sup>, B. Bazi<sup>31</sup>, F. Borondics<sup>87</sup>, S. Nagasawa<sup>26,27</sup>, G. Nishiyama<sup>11</sup>, K. Nitta<sup>49</sup>, J. Mathurin<sup>88</sup>, T. Matsumoto<sup>52</sup>, I. Mitsukawa<sup>52</sup>, H. Miura<sup>89</sup>, A. Miyake<sup>52</sup>, Y. Miyake<sup>65</sup>, H. Yurimoto<sup>90</sup>, R. Okazaki<sup>91</sup>, H. Yabuta<sup>92</sup>, H. Naraoka<sup>91</sup>, K. Sakamoto<sup>5</sup>, S. Tachibana<sup>11,5</sup>, H. C. Connolly Jr.<sup>93</sup>, D. S. Lauretta<sup>94</sup>, M. Yoshitake<sup>5</sup>, M. Yoshikawa<sup>5,6</sup>, K. Yoshikawa<sup>95</sup>, K. Yoshihara<sup>5</sup>, Y. Yokota<sup>5</sup>, K. Yogata<sup>5</sup>, H. Yano<sup>5,6</sup>, Y. Yamamoto<sup>5,6</sup>, D. Yamamoto<sup>5</sup>, M. Yamada<sup>8</sup>, T. Yamada<sup>5</sup>, T. Yada<sup>5</sup>, K. Wada<sup>8</sup>, T. Usui<sup>5,11</sup>, R. Tsukizaki<sup>5</sup>, F. Terui<sup>96</sup>, H. Takeuchi<sup>5,6</sup>, Y. Takei<sup>5</sup>, A. Iwamae<sup>97</sup>, H. Soejima<sup>5,97</sup>, K. Shirai<sup>5</sup>, Y. Shimaki<sup>5</sup>, H. Senshu<sup>8</sup>, H. Sawada<sup>5</sup>, T. Saiki<sup>5</sup>, M. Ozaki<sup>5,6</sup>, G. Ono<sup>95</sup>, T. Okada<sup>5,98</sup>, N. Ogawa<sup>5</sup>, K. Ogawa<sup>5</sup>, R. Noguchi<sup>99</sup>, H. Noda<sup>100</sup>, M. Nishimura<sup>5</sup>, N. Namiki<sup>100,6</sup>, S. Nakazawa<sup>5</sup>, T. Morota<sup>11</sup>, A. Miyazaki<sup>5</sup>, A. Miura<sup>5</sup>, Y. Mimasu<sup>5</sup>, K. Matsumoto<sup>100,6</sup>, K. Kumagai<sup>5,97</sup>, T. Kouyama<sup>101</sup>, S. Kikuchi<sup>8,100</sup>, K. Kawahara<sup>5</sup>, S. Kameda<sup>70,5</sup>, T. Iwata<sup>5,6</sup>, Y. Ishihara<sup>102</sup>, M. Ishiguro<sup>103</sup>, H. Ikeda<sup>95</sup>, S. Hosoda<sup>5</sup>, R. Honda<sup>104,105</sup>, C. Honda<sup>23</sup>, Y. Hitomi<sup>5,97</sup>, N. Hirata<sup>38</sup>, N. Hirata<sup>23</sup>, T. Hayashi<sup>5</sup>, M. Hayakawa<sup>5</sup>, K. Hatakeda<sup>5,97</sup>, S. Furuya<sup>11</sup>, R. Fukai<sup>5</sup>, A. Fujii<sup>5</sup>, Y. Cho<sup>11</sup>, M. Arakawa<sup>38</sup>, M. Abe<sup>5,6</sup>, S. Watanabe<sup>106</sup>, Y. Tsuda<sup>5</sup>

Samples of the carbonaceous asteroid Ryugu were brought to Earth by the Hayabusa2 spacecraft. We analyzed 17 Ryugu samples measuring 1 to 8 millimeters. Carbon dioxide-bearing water inclusions are present within a pyrrhotite crystal, indicating that Ryugu's parent asteroid formed in the outer Solar System. The samples contain low abundances of materials that formed at high temperatures, such as chondrules and calcium- and aluminum-rich inclusions. The samples are rich in phyllosilicates and carbonates, which formed through aqueous alteration reactions at low temperature, high pH, and water/rock ratios of <1 (by mass). Less altered fragments contain olivine, pyroxene, amorphous silicates, calcite, and phosphide. Numerical simulations, based on the mineralogical and physical properties of the samples, indicate that Ryugu's parent body formed ~2 million years after the beginning of Solar System formation.

The carbonaceous asteroid (162173) Ryugu is a rubble pile formed by the reaccumulation of material ejected from a parent asteroid by a large impact (1). Remote sensing observations have shown that Ryugu is related to hydrous carbonaceous chondrite meteorites (2). However, there are some differences with those meteorites, suggesting later heating and partial dehydration of Ryugu (2, 3). Reflectance spectra are nearly uniform across Ryugu's surface, indicating minimal compositional diversity at its surface (2, 3), except for some boulders (3–5).

We expect samples of Ryugu to retain a record of the formation and early evolution of the parent body and Ryugu itself. We analyzed samples collected by the Hayabusa2 spacecraft (6), seeking to determine (i) when and where in the solar nebula Ryugu's parent asteroid formed, (ii) the initial mineralogy and water ice content, (iii) how these original materials evolved through water-rock reactions, (iv) how the asteroid was heated by the decay of short-lived radionuclides, and (v) how the material was ejected from the parent body by an impact and reaccumulated to form Ryugu.

We analyzed 17 Ryugu particles ranging from 1 to 8 mm in size (the largest particle, C0002, is shown in Fig. 1A, and all particles are shown in fig. S1), consisting of seven particles from chamber A, collected at the first touchdown site (TD1), and 10 particles from chamber C, collected at the second touchdown site (TD2) (6). We refer to these millimeter-sized particles as coarse samples. Finer-grained powder samples (<1 mm in size) (fig. S2) obtained from TD1 and TD2 were also used for reflectance spectroscopy.

## Reflectance spectra

Visible (Vis), near-infrared (NIR), and mid-infrared (MIR) reflectance spectra (wavelength range, 0.4 to 18  $\mu\text{m}$ ) were measured from coarse Ryugu samples packed together (seven particles from TD1 and seven particles from TD2) (fig. S2), from the powder samples (fig. S2), and from samples of the meteorites Orgueil and Tagish Lake. The samples were not exposed to air in the entire analysis procedure (7). MIR and far-infrared (FIR; 17 to 100  $\mu\text{m}$ ) reflectance spectra were also measured in air for sample A0026 and samples of the meteorites Orgueil, Alais, Tagish Lake, and Murchison.

All analyzed Ryugu samples exhibit similar Vis-NIR spectra (Fig. 2A). They have ~2.0 to 2.5% reflectance (at 550 nm), with a slightly red slope of ~0.1 to 0.3%  $\mu\text{m}^{-1}$  (0.48 to 0.86  $\mu\text{m}$ ) and ~0.2 to 0.3%  $\mu\text{m}^{-1}$  (2.0 to 2.5  $\mu\text{m}$ ). There are no strong absorption features blueward of 2.7  $\mu\text{m}$  (Fig. 2A). No 0.7  $\mu\text{m}$  absorption, because of Fe<sup>3+</sup>-rich phyllosilicates (8), was detected. The Ryugu samples have an absorption band (~20% in depth) centered at ~2.71  $\mu\text{m}$  (Fig. 2B), which is due to O–H stretching vibrations in Mg-rich phyllosilicates (9, 10). A weaker absorption band at ~3.1  $\mu\text{m}$  is possibly due to ammoniated salts or other nitrogen (N)-bearing compounds (11). Absorptions at ~3.4 to 3.5  $\mu\text{m}$  are due to aliphatic organics and carbonates, and those at ~3.8 to 3.95  $\mu\text{m}$  are due to carbonates. In the MIR-FIR, the Christiansen feature (a reflectance minimum characteristic of the chemical composition) is present at ~9.1  $\mu\text{m}$ . Reststrahlen bands (reflectance peaks associated with Si–O stretching and bending modes) appear as strong peaks at ~9.8  $\mu\text{m}$ , with a shoulder at ~10.75  $\mu\text{m}$ , and as a doublet at ~22.3  $\mu\text{m}$  (Fig. 2C).

Visible spectra of the touchdown sites were previously obtained with the Optical Navigation Camera Telescope (ONC-T) (3) on the Hayabusa2 spacecraft, at spatial resolution of 0.3 to 0.5 m per pixel, before and after the sample collection. The location of TD1 showed higher reflectance than that of TD2 (Fig. 2D). We found similar results: The coarse and powder Ryugu samples from TD1 both exhibit higher reflectance than those from TD2 (Fig. 2A). The surface reflectance decreased after



the touchdowns because the spacecraft thrusters removed powder from the surface of Ryugu during ascent (Fig. 2D) (12). Visible spectra of the coarse and powder Ryugu samples have similar reflectance values to those of the ONC-T spectra of the landing sites (7) and to the global average (Fig. 2A); the reflectance ratios of ONC-T to the powder samples at 0.55  $\mu\text{m}$  are  $\sim 0.9$  for both TD1 and TD2 (Fig. 2D). This indicates that the samples are representative of the global reflectance properties of Ryugu.

Spectra of the Ryugu samples are generally consistent with Ryugu average spectra measured with Hayabusa2's ONC-T (3) and Near Infrared Spectrometer (NIRS3) (2) instruments. There are some differences between the NIRS3 and laboratory spectra (Fig. 2A), even after converting both to the same wavelength resolution (Fig. 2B). The NIRS3 spectra have lower reflectance  $R$  relative to sample ( $R_{\text{NIRS3}}/R_{\text{sample}} = 0.7$  at 2.0  $\mu\text{m}$ ) and a shallower 2.7  $\mu\text{m}$  absorption depth (ratio of  $\sim 0.5$  at 2.7  $\mu\text{m}$ ), which is con-

sistent with analysis of other Ryugu samples (13). This could be due to differences in particle size distribution and porosity between the laboratory samples and Ryugu's surface or to the much larger field of view of NIRS3 (13).

Spectra of Ryugu and the laboratory samples have similar reflectances to that of asteroid Bennu (14) at visible wavelengths, but opposite spectral slopes (Fig. 2A). The 2.7  $\mu\text{m}$  feature (Fig. 2B) and the bands in the MIR-FIR spectrum (Fig. 2C) of Bennu (15) also differ from Ryugu.

The Ryugu samples are much darker and have a flatter spectral slope than the meteorites Orgueil and Tagish Lake (Fig. 2A). Orgueil is classified as a CI1 meteorite, meaning an aqueously altered (modified by reactions with water) Ivuna-type carbonaceous chondrite, whereas Tagish Lake is a C2, a carbonaceous chondrite that was less altered so retains anhydrous minerals. The position of the OH absorption band in the Ryugu sample spectra is

consistent with that in Orgueil, Tagish Lake, and Flensburg. Flensburg is an ungrouped C1 chondrite, in which chondrules (submillimeter anhydrous aggregates made of silicate and glass) are totally replaced by phyllosilicates (16). The same feature appears at longer wavelengths in Murchison, which is classified as CM2 (carbonaceous chondrite meteorites of Mighei type), and in asteroid Bennu (Fig. 2B) (2, 14). The position of this band is known to correlate with the Mg/Fe ratio in phyllosilicates, so we infer that Ryugu, Orgueil, Tagish Lake, and Flensburg contain Mg-rich phyllosilicates, whereas Murchison and Bennu contain Fe-rich phyllosilicates (9, 10).

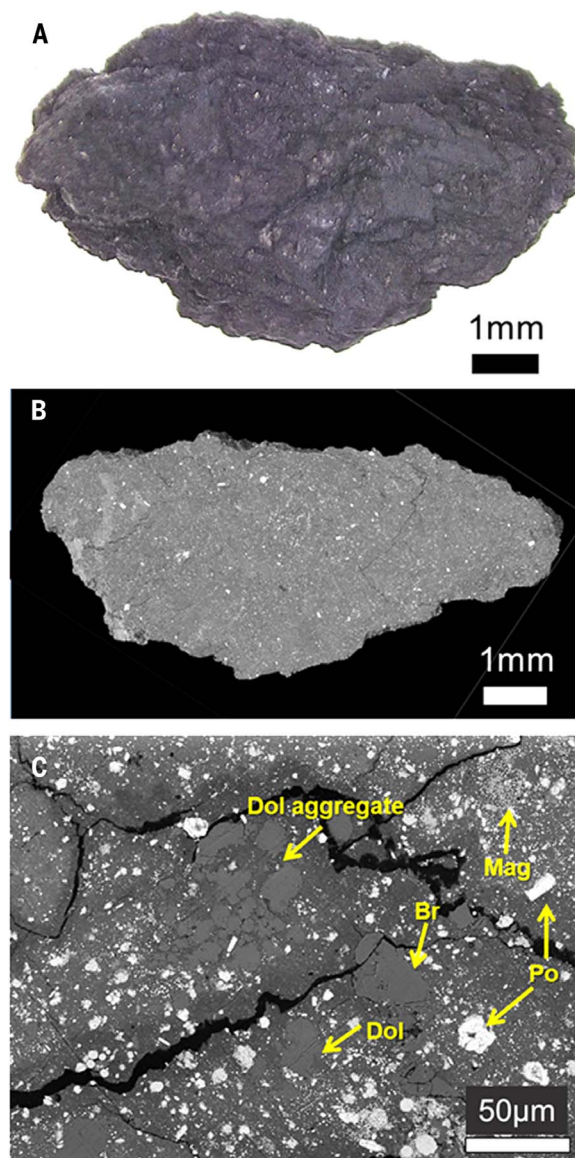
### Three-dimensional structure and density

All but one of our coarse Ryugu samples (the exception was sample A0058) were characterized by using synchrotron x-ray computed tomography (SR-CT) (7), with a resolution of 0.85  $\mu\text{m}$  per voxel (table S1). Most of the

<sup>1</sup>Department of Earth Sciences, Tohoku University, Sendai 980-8578, Japan. <sup>2</sup>NASA Johnson Space Center, Houston, TX 77058, USA. <sup>3</sup>The University Museum, The University of Tokyo, Tokyo 113-0033, Japan. <sup>4</sup>Earth-Life Science Institute, Tokyo Institute of Technology, Tokyo 152-8550, Japan. <sup>5</sup>Institute of Space and Astronautical Science, Japan Aerospace Exploration Agency (JAXA), Sagami-hara 252-5210, Japan. <sup>6</sup>Department of Space and Astronautical Science, The Graduate University for Advanced Studies (SOKENDAI), Hayama 240-0193, Japan. <sup>7</sup>School of Earth and Space Exploration, Arizona State University, Tempe, AZ 85287, USA. <sup>8</sup>Planetary Exploration Research Center, Chiba Institute of Technology, Narashino 275-0016, Japan. <sup>9</sup>Department of Earth, Atmospheric and Planetary Sciences, Massachusetts Institute of Technology, Cambridge, MA 02139, USA. <sup>10</sup>Department of Mechanical Systems Engineering, Nagoya University, Nagoya 464-8603, Japan. <sup>11</sup>Department of Earth and Planetary Science, The University of Tokyo, Tokyo 113-0033, Japan. <sup>12</sup>Isotope Science Center, The University of Tokyo, Tokyo 113-0032, Japan. <sup>13</sup>Laboratoire d'Etudes Spatiales et d'Instrumentation en Astrophysique (LESIA), Observatoire de Paris, Meudon 92195 France. <sup>14</sup>Geological Survey of Japan, National Institute of Advanced Industrial Science and Technology (AIST), Tsukuba, 305-8567, Japan. <sup>15</sup>Department of Earth and Planetary Sciences, University of New Mexico, Albuquerque, NM 87131, USA. <sup>16</sup>Research Organization of Science and Technology, Ritsumeikan University, Kusatsu 525-8577, Japan. <sup>17</sup>Key Laboratory of Mineralogy and Metallogeny, Guangzhou Provincial Key Laboratory of Mineral Physics and Materials, Guangzhou Institute of Geochemistry, Chinese Academy of Sciences (CAS), Guangzhou 510640, China. <sup>18</sup>Center for Excellence in Deep Earth Science, CAS, Guangzhou 510640, China. <sup>19</sup>Scattering and Imaging Division, Japan Synchrotron Radiation Research Institute, Sayo 679-5198, Japan. <sup>20</sup>Institute of Low Temperature Science, Hokkaido University, Sapporo 060-0819, Japan. <sup>21</sup>Department of Earth, Environmental, and Planetary Sciences, Brown University, Providence, RI 02912, USA. <sup>22</sup>Instituto de Astrofísica de Canarias, University of La Laguna, Tenerife 38205, Spain. <sup>23</sup>Aizu Research Center for Space Informatics, The University of Aizu, Aizu-Wakamatsu 965-8580, Japan. <sup>24</sup>Department of Astronomy, University of Washington, Seattle, WA 98195 USA. <sup>25</sup>Institute for Radiation Sciences, Osaka University, Toyonaka 560-0043, Japan. <sup>26</sup>Kavli Institute for the Physics and Mathematics of the Universe, The University of Tokyo, Kashiwa 277-8583, Japan. <sup>27</sup>Department of Physics, The University of Tokyo, Tokyo 113-0033, Japan. <sup>28</sup>Materials Sciences Research Center, Japan Atomic Energy Agency, Tokai 319-1195, Japan. <sup>29</sup>Department of Earth and Space Science, Osaka University, Toyonaka 560-0043, Japan. <sup>30</sup>Institute of Geoscience, Goethe University, Frankfurt, 60438 Frankfurt am Main, Germany. <sup>31</sup>Department of Chemistry, Ghent University, Krijgslaan 281 S12, Ghent, Belgium. <sup>32</sup>Institut d'Astrophysique Spatiale, Université Paris-Saclay, Orsay 91405, France. <sup>33</sup>Department of Earth Sciences, Royal Holloway, University of London, Egham TW20 0EX, UK. <sup>34</sup>Institut de Minéralogie, Physique des Matériaux et Cosmochimie, Muséum National d'Histoire Naturelle, Centre national de la recherche scientifique (CNRS), Sorbonne Université, Paris, France. <sup>35</sup>Institut de Planétologie et d'Astrophysique de Grenoble, CNRS, Université Grenoble Alpes, 38000 Grenoble, France. <sup>36</sup>Advanced Photon Source, Argonne National Laboratory, Argonne, IL 60439, USA. <sup>37</sup>Faculty of Engineering, Kindai University, Higashi-Hiroshima 739-2116, Japan. <sup>38</sup>Department of Planetology, Kobe University, Kobe 657-8501, Japan. <sup>39</sup>Department of Earth Resources Engineering, Kyushu University, Fukuoka 819-0395, Japan. <sup>40</sup>School of Engineering, The University of Tokyo, Tokyo 113-0033, Japan. <sup>41</sup>Department of Physics, Kwansei Gakuin University, Sanda 669-1330, Japan. <sup>42</sup>Department of Earth and Atmospheric Sciences, University of Houston, Houston, TX 77204, USA. <sup>43</sup>Texas Materials Institute, The University of Texas at Austin, Austin, TX 78712, USA. <sup>44</sup>Department of Geoscience, Virginia Tech, Blacksburg, VA 24061, USA. <sup>45</sup>Materials Analysis Station, National Institute for Materials Science, Tsukuba 305-0047, Japan. <sup>46</sup>Institute for Materials Research, Tohoku University, Sendai 980-8577, Japan. <sup>47</sup>Department of Earth Science, Natural History Museum, London SW7 5BD, UK. <sup>48</sup>Institute of Nature and Environmental Technology, Kanazawa University, Kanazawa 920-1192, Japan. <sup>49</sup>Spectroscopy Division, Japan Synchrotron Radiation Research Institute, Sayo 679-5198, Japan. <sup>50</sup>Department of Materials Structure Science, The Graduate University for Advanced Studies (SOKENDAI), Tsukuba, Ibaraki 305-0801, Japan. <sup>51</sup>Institute of Materials Structure Science, High-Energy Accelerator Research Organization, Tsukuba 305-0801, Japan. <sup>52</sup>Division of Earth and Planetary Sciences, Kyoto University, Kyoto 606-8502, Japan. <sup>53</sup>Faculty of Arts and Science, Kyushu University, Fukuoka 819-0395, Japan. <sup>54</sup>Planetary Science Institute, Tucson, AZ 85719, USA. <sup>55</sup>The Pennsylvania State University, University Park, PA 16802, USA. <sup>56</sup>Department of Physics, California State University, San Marcos, CA 92096, USA. <sup>57</sup>Space Sciences Laboratory, University of California, Berkeley, CA 94720, USA. <sup>58</sup>Laboratoire de Physique des 2 Infinis Irène Joliot-Curie, Université Paris-Saclay, CNRS, 91405 Orsay, France. <sup>59</sup>Institute for Planetary Research, Deutsches Zentrum für Luftund Raumfahrt, Rutherfordstraße 2 12489 Berlin, Germany. <sup>60</sup>Division of Geological and Planetary Sciences, California Institute of Technology, Pasadena CA 91125, USA. <sup>61</sup>Department of Geosciences, Shizuoka University, Shizuoka 422-8529, Japan. <sup>62</sup>Department of Materials Science and Engineering, Tokyo Institute of Technology, Tokyo 152-8550, Japan. <sup>63</sup>Graduate School of Science and Engineering, Ehime University, Matsuyama 790-8577, Japan. <sup>64</sup>European Space Astronomy Centre, 28692 Villanueva de la Cañada, Spain. <sup>65</sup>High Energy Accelerator Research Organization, Tokai 319-1106, Japan. <sup>66</sup>Department of Applied Physics, Osaka University, Suita 565-0871, Japan. <sup>67</sup>Hitachi, Hatoyama 350-0395, Japan. <sup>68</sup>Institute for Integrated Radiation and Nuclear Science, Kyoto University, Kumatori 590-0494, Japan. <sup>69</sup>National Metrology Institute of Japan, AIST, Tsukuba 305-8565, Japan. <sup>70</sup>Department of Physics, Rikkyo University, Tokyo 171-8501, Japan. <sup>71</sup>Japan Fine Ceramics Center, Nagoya 456-8587, Japan. <sup>72</sup>Toyota Central Research and Development Laboratories, Nagakute 480-1192, Japan. <sup>73</sup>Instituto di Astrofisica e Planetologia Spaziali, Istituto Nazionale di Astrofisica, Rome 00133, Italy. <sup>74</sup>Institut Universitaire de France, Paris, France. <sup>75</sup>Faculty of Aerospace Engineering, Delft University of Technology, Delft, Netherlands. <sup>76</sup>Department of Physical Sciences, Ritsumeikan University, Shiga 525-0058, Japan. <sup>77</sup>Physical Sciences Laboratory, The Aerospace Corporation, CA 90245, USA. <sup>78</sup>University of Chinese Academy of Sciences, Beijing 100049, China. <sup>79</sup>Institut des Sciences Moléculaires d'Orsay, Université Paris-Saclay, CNRS, 91405 Orsay, France. <sup>80</sup>Deutsches Elektronen-Synchrotron Photon Science, 22603 Hamburg, Germany. <sup>81</sup>Nano Life Science Institute, Kanazawa University, Kanazawa 920-1192, Japan. <sup>82</sup>Graduate School of Life Science, University of Hyogo, Hyogo 678-1297, Japan. <sup>83</sup>Institut de Physique du Globe de Paris, Université de Paris, Paris 75205, France. <sup>84</sup>Division of Natural Sciences, International Christian University, Mitaka 181-8585, Japan. <sup>85</sup>Institute of Geosciences, Friedrich-Schiller-Universität Jena, 07745 Jena, Germany. <sup>86</sup>Center for Advanced Radiation Sources, University of Chicago, Chicago, IL 60637, USA. <sup>87</sup>Optimized Light Source of Intermediate Energy to LURE (SOLEIL) L'Orme des Merisiers, Gif sur Yvette F-91192, France. <sup>88</sup>Institut Chimie Physique, Université Paris-Saclay, CNRS, 91405 Orsay, France. <sup>89</sup>Graduate School of Science, Nagoya City University, Nagoya 467-8501, Japan. <sup>90</sup>Department of Natural History Sciences, Hokkaido University, Sapporo 060-0810, Japan. <sup>91</sup>Department of Earth and Planetary Sciences, Kyushu University, Fukuoka 819-0395, Japan. <sup>92</sup>Graduate School of Advanced Science and Engineering, Hiroshima University, Higashi-Hiroshima 739-8526, Japan. <sup>93</sup>Department of Geology, Rowan University, Glassboro, NJ 08028, USA. <sup>94</sup>Lunar and Planetary Laboratory, University of Arizona, Tucson, AZ 85721, USA. <sup>95</sup>Research and Development Directorate, JAXA, Sagami-hara 252-5210, Japan. <sup>96</sup>Department of Mechanical Engineering, Kanagawa Institute of Technology, Atsugi 243-0292, Japan. <sup>97</sup>Marine Works Japan, Yokosuka 237-0063, Japan. <sup>98</sup>Department of Chemistry, The University of Tokyo, Tokyo 113-0033, Japan. <sup>99</sup>Faculty of Science, Niigata University, Niigata 950-2181, Japan. <sup>100</sup>National Astronomical Observatory of Japan, Mitaka 181-8588, Japan. <sup>101</sup>Digital Architecture Research Center, National Institute of Advanced Industrial Science and Technology, Tokyo 135-0064, Japan. <sup>102</sup>JAXA Space Exploration Center, JAXA, Sagami-hara 252-5210, Japan. <sup>103</sup>Department of Physics and Astronomy, Seoul National University, Seoul 08826, Korea. <sup>104</sup>Department of Information Science, Kochi University, Kochi 780-8520, Japan. <sup>105</sup>Center for Data Science, Ehime University, Matsuyama 790-8577, Japan. <sup>106</sup>Department of Earth and Environmental Sciences, Nagoya University, Nagoya 464-8601, Japan.

\*Corresponding author. Email: tomoki.nakamura.a8@tohoku.ac.jp

**Fig. 1. Morphology and internal texture of C0002. (A)** Optical micrograph of entire C0002 sample. **(B)** CT image of the largest cross section, showing the absence of chondrules and CAIs. **(C)** Back-scattered electron (BSE) image of typical internal texture. Dolomite (Dol), breunnerite (Br), pyrrhotite (Po), and magnetite framboids (Mag) are labeled; these are embedded in a fine-grained phyllosilicate matrix.



samples had an irregular shape, but some exhibited one or two broad flat surfaces. Particles with flat surfaces were also observed during the sample collection process (6). The particle interiors have cracks; most are irregular, but some particles (such as C0055) contain parallel cracks with spacings of tens to hundreds of micrometers (fig. S3).

The mass of each coarse sample particle was measured under dry conditions in a glove box, and the density was calculated from the sample volume determined by using SR-CT (table S1). The bulk density (mass per total volume, including cracks and pores) ranged from 1.7 to 1.9 g cm<sup>-3</sup> with an average of 1.79 ± 0.08 g cm<sup>-3</sup> (table S1), which is higher than was estimated from earlier measurements in the curation facility (1.3 g cm<sup>-3</sup>) (17), which did not consider the full three-dimensional (3D) structure. These densities are higher than the measured average density of Ryugu (1.2 g cm<sup>-3</sup>) (1), indicating

that the asteroid has high internal macroporosity. The average bulk densities of CI (Ivuna-type) and CM (Mighei-type) chondrite meteorites are 2.12 and 2.21 g cm<sup>-3</sup>, respectively (18), whereas the ungrouped CI chondrite Flensburg has a density of 1.98 g cm<sup>-3</sup> (16). Because Ryugu has mineralogical similarities to CI chondrites, the lower density of the Ryugu samples indicates a higher porosity than that of CI chondrites.

#### Mechanical, thermal, electrical, and magnetic properties

The Ryugu samples A0026 (TD1) and C0002 (TD2; our largest particle) were measured (7) to determine mechanical, thermal, electrical, and magnetic properties (Table 1) to compare with carbonaceous chondrites (table S2) and for use in numerical simulations.

The resulting physical properties of the Ryugu samples are not identical to any known meteor-

ite. Most properties are similar to hydrous CI and CM chondrites but differ from anhydrous CV (Vigarano-type) and CO (Ornans-type) chondrites (Table 1 and table S2). The mechanical properties show that Ryugu samples are weaker in strength, especially their Young's modulus and Poisson's ratio, than hydrous carbonaceous chondrites (table S2) and have a larger volume change upon deformation (such as compression or impact). The thermal expansivity of the Ryugu samples differs from the nonlinear temperature-dependent results measured for some carbonaceous chondrites (19) but is linear in the temperature range of 220 to 370 K (fig. S4).

The thermal properties (Table 1) could be responsible for the low thermal inertia of Ryugu (20, 21). The thermal diffusivity (Table 1) and the bulk density of sample C0002 (table S1) were used to calculate the thermal conductivity of 0.5 W m<sup>-1</sup> K<sup>-1</sup> and thermal inertia of 890 J m<sup>-2</sup> s<sup>-0.5</sup> K<sup>-1</sup> [hereafter thermal inertia units (TIU)] at a temperature of 298 K. The thermal inertia of the sample is higher than the mean of the asteroid surface observed by Hayabusa2 [225 ± 45 TIU (22)] and measured in situ by the Mobile Asteroid Surface Scout (MASCOT) [295 ± 18 TIU (21)]. Remote sensing is sensitive to a thermal skin depth of ~10 mm, whereas the thickness of the sample measured in the laboratory is <1 mm, so a thermal shielding effect could arise on intermediate scales (for example, cracks of several millimeters in length).

Thin sections of magnetite framboids (aggregates of equidimensional microcrystals of magnetite) with diameters of 300 to 1100 nm were observed with electron holography at a spatial resolution of 14 nm (7). These magnetite inclusions have vortex magnetic structures and magnetic flux leakage out of the particles (Fig. 3, A to C, and fig. S5). The externally leaking magnetic flux was detected as remanent magnetization in macroscopic measurements. Mössbauer spectra showed that half of the iron in these samples is in magnetite, and the magnetic hysteresis parameter values (Table 1) are similar to those of carbonaceous chondrites that contain submicrometer magnetite framboids (23, 24). Therefore, the magnetite framboids dominate the natural remanent magnetization (NRM) of asteroid Ryugu. Two Ryugu particles from different sampling sites (A0026 from TD1 and C0002 from TD2) record magnetic fields of 31 to 260 µT and 18 to 704 µT (fig. S6), respectively. We suggest that the source magnetic field was homogeneous on Ryugu's parent body.

#### Elemental abundances

We used muon x-ray emission spectroscopy to measure the abundances of major chemical elements in 10 coarse Ryugu samples, including the largest sample C0002 (126.6 mg in total)



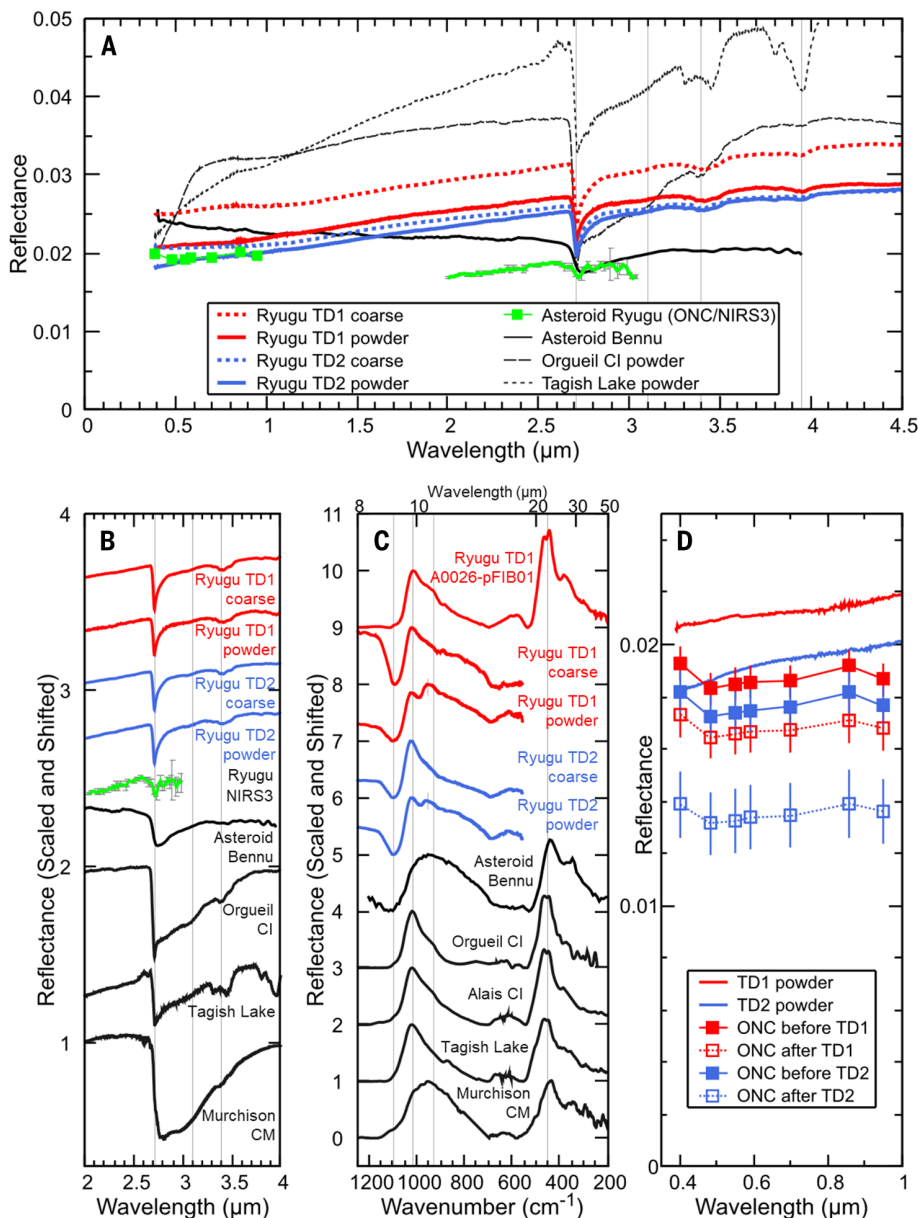


**Fig. 2. Reflectance spectra of coarse and powder samples of Ryugu.** (A) Vis-NIR reflectance spectra of coarse (dotted lines) and powder (solid lines) samples from the TD1 (red) and TD2 (blue) sites on Ryugu, compared with hydrated carbonaceous chondrites (dashed and dotted black lines), Hayabusa2 remote sensing observations of Ryugu (solid green lines) (2, 3), and remote sensing observations of Benu (solid black line) (14). The vertical gray lines are at 2.71, 3.1, 3.4, and 3.95  $\mu\text{m}$ . (B) Same data as (A), but normalized at 2.595  $\mu\text{m}$  and shifted arbitrarily in the NIR wavelength region to aid comparison. (C) MIR-FIR spectra of TD1 and TD2 coarse and powder samples, the flat surface of sample A0026, remote sensing observations of Benu (95), pressed powders of meteorites (Alais and Tagish Lake), and meteorite coarse samples (Orgueil and Murchison). All spectra are scaled to have the same difference between reflectance minimum and maximum, then shifted arbitrarily for comparison. The vertical gray lines at 9.1, 9.8, 10.75, and 22.3  $\mu\text{m}$  indicate, respectively, the Christiansen feature, an Si-O stretching peak, an additional shoulder of the main Si-O peak, and a peak of the doublet from saponite (96). The peaks at 10.5  $\mu\text{m}$  in the powder samples are scattered light from the sample dish (7). (D) Visible reflectance spectra of Ryugu TD1 and TD2 powder samples measured in the laboratory compared with the TD1 and TD2 sites before and after the touchdowns (7).

(7, 25, 26). Because the muon beam is  $>3$  cm in diameter, we analyzed all 10 samples together to obtain a mean bulk elemental abundance. Pellets of the meteorites Murray (type CM2;

306.5 mg) and Orgueil (type CI1; 195 mg) were measured for comparison.

We detected carbon (C), N, oxygen (O), sodium (Na), magnesium (Mg), silicon (Si), sul-

fur (S), iron (Fe), and nickel (Ni) (Fig. 4A). The Ryugu and Orgueil spectra are very similar, indicating similar major elemental abundances. However, the Ryugu samples contain less O than that in Orgueil.

We calculated elemental mass ratios  $M/\text{Si}$  ( $M = \text{C}, \text{N}, \text{O}, \text{Na}, \text{Mg}, \text{S}, \text{and Fe}$ ) from the muon x-ray data (7).  $M/\text{Si}$  has previously been measured for the Murray meteorite (table S3), so it was used as a standard. We determined Ryugu mass ratios of  $\text{C}/\text{Si} = 0.338 \pm 0.008$ ,  $\text{N}/\text{Si} = 0.019 \pm 0.009$ ,  $\text{O}/\text{Si} = 3.152 \pm 0.099$ ,  $\text{Na}/\text{Si} = 0.039 \pm 0.006$ ,  $\text{Mg}/\text{Si} = 0.890 \pm 0.021$ ,  $\text{S}/\text{Si} = 0.510 \pm 0.019$ , and  $\text{Fe}/\text{Si} = 1.620 \pm 0.040$ . These elemental ratios are consistent with those of CI chondrites (27) and the Sun (28), except O/Si is 25% lower in Ryugu than in CIs (table S3 and fig. S7). These abundances are nevertheless sufficiently similar to classify Ryugu as a CI chondrite, which is consistent with other lines of evidence (29).

CI chondrites contain 45 wt % oxygen (27); Ryugu is therefore depleted in oxygen by 11.3 wt %, given its similar Si concentration to CI chondrites (29). The Ryugu samples were prepared and analyzed in low-oxygen conditions ( $<0.1\%$ ) and in dry atmosphere (dew points  $< -50^\circ\text{C}$ ), so the results indicate the indigenous oxygen abundance of Ryugu. The lower water content and sulfate abundance of Ryugu samples than CI chondrites (29) are probably the cause of the low oxygen abundance.

Nitrogen-bearing molecules such as  $\text{NH}_3$ , CN, and  $\text{N}_2$  have low freezing points and could only have been incorporated into asteroids in the outer Solar System (30). The N/C ratio can therefore be used to infer the distance from the Sun of Ryugu's parent body during its formation. We measured an average N/C atomic ratio of  $0.047 \pm 0.022$  from the 10 coarse samples. This is higher than that of primitive anhydrous chondrites (N/C = 0.001 to 0.02), which is consistent with hydrated chondrites such as CM and CI (N/C = 0.02 to 0.06) and lower than ultracarbonaceous micrometeorites of probable cometary origin (N/C = 0.06 to 0.2) (30). We conclude that Ryugu's parent body formed at heliocentric distances similar to those of hydrated carbonaceous chondrites.

### Mineralogy and mineral chemistry

The SR-CT image of C0002 (Fig. 1B) shows that it consists almost entirely of fine-grained matrix material. We searched for distinct objects formed at high temperatures ( $>1000^\circ\text{C}$ ) in the early solar nebula, such as chondrules (formed by melting of precursor silicate-rich dust) or Ca-, aluminum (Al)-rich inclusions (CAIs; formed through condensation from hot nebular gas and the earliest solids to form in the Solar System). We found no examples more than 100  $\mu\text{m}$  in diameter in any of the

Table 1. Summary of the physical properties measured from the Ryugu samples (7).

Value	Uncertainty	Unit	Measurement condition	Measured sample(s)	
<i>Mechanical properties</i>					
Compressive hardness	0.18	0.1	GPa	Ambient	C0002 plate 3*
Young's modulus	5.3	1.6	GPa	Ambient	C0002 plate 3*
Bending strength	4.9	1.9	MPa	Ambient	C0002 plate 3 and 4
Longitudinal velocity	2.08	0.13	km/s	Ambient	Average of C0002 plate 3 and 4†
Shear velocity	1.37	0.15	km/s	Ambient	Average of C0002 plate 3 and 4†
Thermal expansivity	$2.6 \times 10^{-5}$	$2 \times 10^{-6}$	/K	210 to 400 K, nitrogen gas	C0002 plate 3
Cohesive force	0.17	0.02	$\mu\text{N}$	Ambient	C0002 plate 4
<i>Thermal properties</i>					
Heat capacity at 298K	865	16	J/kg/K	213 to 373 K, nitrogen gas	Average of C0002 plate 4 and A0026
Thermal diffusivity	$3.2 \times 10^{-7}$	$0.3 \times 10^{-7}$	$\text{m}^2/\text{s}$	300 K, vacuum	Average of C0002 plate 3 and 4
<i>Electrical properties</i>					
Resistivity	$2.5 \times 10^6$	$0.3 \times 10^{-6}$	ohm·m	300 K, vacuum	Average of C0002 plate 3 and 4
Relative permittivity	6.8	0.8	—	300 K, vacuum	Average of C0002 plate 3 and 4
<i>Magnetic properties</i>					
Magnetic susceptibility	$8.39 \times 10^{-5}$	$4.0 \times 10^{-6}$	$\text{m}^3/\text{kg}$	300 K, direct current, alternating current (1 to 1000 Hz)	Average of C0002 and A0026
Saturation magnetization	11.6	$5.1 \times 10^{-3}$	$\text{Am}^2/\text{kg}$	300 K	Average of C0002 and A0026
Saturation remanence	1.05	$6.3 \times 10^{-3}$	$\text{Am}^2/\text{kg}$	300 K	Average of C0002 and A0026
Coercivity	12.2	$9.3 \times 10^{-2}$	mT	300 K	Average of C0002 and A0026
Coercivity of remanence	61.3	$4.1 \times 10^{-1}$	mT	300 K	Average of C0002 and A0026

\*Average is of 26 analyses of fine-grained matrix.

†Two fragments from plate 4 were used.

coarse samples, but there are smaller examples. CI chondrites also lack large chondrules.

We produced 31 polished sections cut from 11 samples (table S4), including two plates from the largest sample C0002. Observations with field-emission electron microscopes show that most of the coarse samples are breccias—rocks that consist of fragments ranging in size from ~10 to ~500  $\mu\text{m}$ . Elemental abundance maps of Na and Mg show compositional differences between fragments (fig. S8), usually with sharp boundaries. Most of the fragments consist primarily of fine-grained matrix material, with similar (although not identical) mineralogy and mineral chemistry, which we refer to as Ryugu's major lithology. CI1 chondrites have similar properties, with Orgueil being the most brecciated (31, 32). The Ryugu samples have similar levels of brecciation to that of Orgueil.

The major lithology of Ryugu (Fig. 1C) consists of minerals formed through aqueous alteration: The dominant phase is a phyllosilicate-rich matrix that contains minerals including abundant iron sulfides (pyrrhotite and pentlandite), carbonates (breunnerite and dolomite), magnetite, and hydroxyapatite. The phyllosilicates consist of the minerals saponite and serpentine. Chlorite was only detected in a limited area in C0076. Mg–Na phosphate occurs in some places and appears to have shrunk in volume since its formation, probably owing to degassing of volatile species, such as water (fig.

S9). Dolomite is the most abundant carbonate mineral; breunnerite is less abundant but occurs as larger crystals, with one in C0002 measuring 940 by 450 by 262  $\mu\text{m}$  (movie S1). Ca carbonate is rare. Pyrrhotite crystals with a pseudohexagonal shape (1 to 100  $\mu\text{m}$ ) are abundant and sometimes include pentlandite. Nano- to submicrometer-size pyrrhotite and pentlandite crystals occur ubiquitously in the phyllosilicate matrix (fig. S10). Magnetite is present in diverse morphologies (fig. S11), which is typical of CI1 chondrites (31). The carbonates often contain small (<10  $\mu\text{m}$ ) crystals of magnetite and pyrrhotite. Small (<10  $\mu\text{m}$ ) olivine and low-Ca pyroxene crystals are present but rare; they are completely absent from some of the coarse samples.

Ferrihydrate was not observed, despite being a major component of Orgueil (33, 34). Nor was magnesium sulfate. Calcium sulfate [gypsum;  $\text{CaSO}_4 \cdot 2(\text{H}_2\text{O})$ ] was detected only as very small grains around larger crystals of calcite (fig. S12); it probably formed after sample recovery on Earth, through reactions of calcite with sulfuric acid, produced by oxidation of small pyrrhotite crystals within the Ryugu samples (35, 36). Small crystals of sodium sulfate grew on the surface of polished sections of Ryugu samples (fig. S13) so are of terrestrial origin. We infer that sulfates are likely absent on Ryugu, implying that sulfates in CI1 chondrites are terrestrial contamination (37). Additional minor minerals include chromite, manganese

(Mn)-rich ilmenite, spinel, zinc sulfide (ZnS), cubanite, and daubréelite. Carbonaceous material occurs as globules and diffuse objects embedded in the matrix.

Phyllosilicates in the major lithology have Mg# [defined as the atomic ratio  $\text{Mg}/(\text{Mg}+\text{Fe}) \times 100$ ] mostly in the range of 75 to 90, which is similar to that in Orgueil. However, Ryugu phyllosilicates have more Mg-rich varieties than in Orgueil, with some locations having  $\text{Mg}\# > 85$  (Fig. 4B). The compositions of the carbonates are very similar to those of CI1 chondrites (Fig. 4C). Breunnerite and dolomite contain 1 to 10 wt % and 2 to 5 wt % MnO, respectively. Hydroxyapatite contains a small amount of fluorine (<1 wt %), which is typical of chondrites (38). We performed high-energy synchrotron x-ray fluorescence (XRF) tomographic analysis (39) and found enrichment of rare-earth elements (REEs) in hydroxyapatite, with mutually consistent levels of each REE (fig. S14). This is unlike apatite grains in ordinary chondrites (40) and Orgueil (32), which have higher levels of europium (Eu) and gadolinium (Gd), respectively, than those of other REEs. Ordinary chondrites and CK (Karoonda-type carbonaceous) chondrites have REE abundances that decrease from light to heavy atomic masses (40), unlike Ryugu. The magnetite does not contain detectable trace elements, whereas ilmenite contains various concentrations of MnO up to 10 wt %, both of which are typical of CIs (34, 41). Pyrrhotite



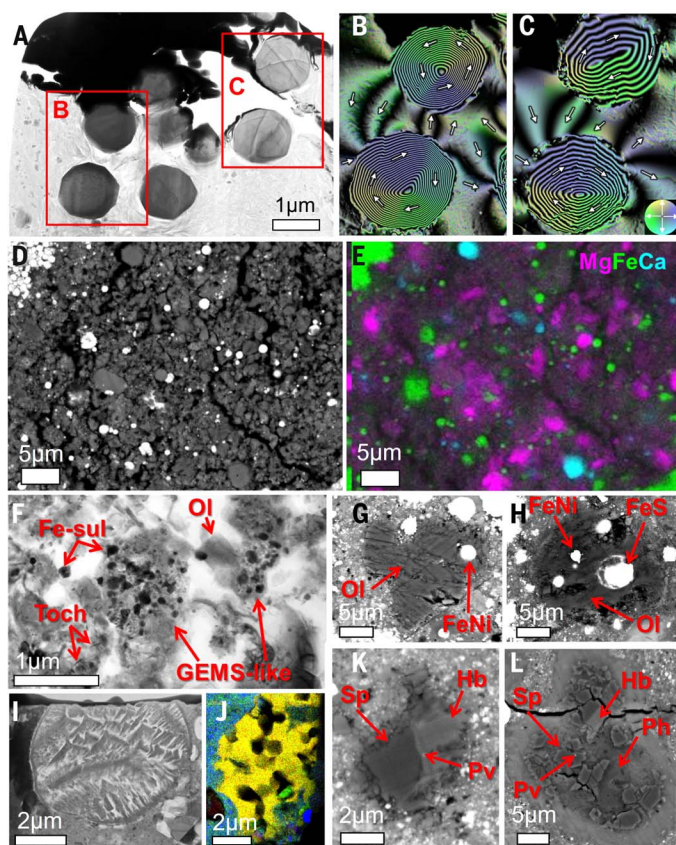


**Fig. 3. Characteristic textures, magnetic structures, and embedded objects in the Ryugu samples.**

(A) TEM image of typical magnetite framboids (dark gray rounded objects) from A0064. The light gray area is phyllosilicate from the major lithology, and the upper black area is tungsten contamination. (B and C) Color maps of the magnetic flux direction obtained from the reconstruction of remanent magnetism, for the magnetite framboids in red boxes in (A) observed by using electron holography (7). Each particle has a concentric circular magnetic field (vortex structure) indicated with white arrows, which show the direction of the magnetic flux as shown in the color-wheel in (C). The composition and electron diffraction data for this region are shown in fig. S5. (D) Enlarged view of the least-altered fragment 4 in sample C0002, showing high porosity. (E) Compositional map of (D), showing high abundances of Mg-rich olivine and Mg-rich, low-Ca pyroxene (magenta); magnetite and pyrrhotite (green); and minor Ca carbonate (light blue). (F) TEM image of a part of the least-altered fragment 5 in C0002, showing a very porous aggregate with labeled GEMS-like objects, Fe sulfide (Fe-sul), Mg-rich olivine (Ol), and tochilinite (Toch). (G to I) Chondrule-like objects. Objects in (G) and (H), both from C0002, show textures similar to those of type I chondrules, consisting of Mg-rich olivine (Ol) and an FeNi metal inclusion. An FeS inclusion occurs only in (H). The object in (I), from C0076, shows a barred-olivine texture, consisting of several sets of parallel olivine bars and an olivine rim. (J) TEM-energy-dispersive spectrometer (EDS) color map of a porous olivine (yellow) from C0076, including a small Al-, Ti-rich diopside crystal (green). Red-green-blue (RGB) colors indicate the concentrations of Mg, Si, and Fe, respectively. (K and L) Small CAI-like objects. The object in (K), from C0040, consists of Al spinel (Sp), hibonite (Hb), and a small inclusion of perovskite (Pv). The object in (L), from C0002, consists of Al spinel (Sp), hibonite (Hb), a small inclusion of perovskite (Pv), and phyllosilicate (Ph). (A), (F), and (I) are bright-field TEM images, and (D), (G), (H), (K), and (L) are BSE images.

contains Ni up to 2 wt %. The Ni/Fe atomic ratios of pentlandite range from 1 to 1.2 in most cases. Representative compositions are listed in table S5.

Relative mineral abundances were estimated from two element maps of C0002 (~9.0 and ~8.6 mm<sup>2</sup> area) composed primarily of the major lithology. The abundances (table S6) are broadly consistent with those of Orgueil (31, 32, 42).

We performed x-ray diffraction (XRD) analysis of a whole sample of C0002 (fig. S15) and found a large, broad peak at ~10 Å and a distinct peak at 7.45 Å, which we identified as being due to saponite and serpentine, respectively. The 10-Å peak indicates a low abundance of interlayer H<sub>2</sub>O in saponite, as previously inferred from use of other techniques (29). To characterize the phyllosilicates, we applied ethylene glycol to 10 small particles separated

from several coarse samples (7) and observed peak shifts in the XRD patterns, indicating expansion of interlayer spacings due to incorporation of glycol (fig. S16). We identified reflections at 16.8 and 13.3 Å as being due to saponite-serpentine mixed-layer minerals, and at 7.28 Å as being due to pure serpentine (7). The saponite-rich mixed-layer mineral is the most abundant, followed by serpentine, but the relative abundances differ between samples. Similar results have previously been obtained for Orgueil (43).

Although the bulk mineralogy of Ryugu samples is similar to that of Orgueil, we found that the Ryugu samples are much darker. Possible explanations are the presence of bright Mg-sulfate epsomite in Orgueil (37), or a lower Fe<sup>3+</sup> abundance in phyllosilicates in the Ryugu samples (Fe<sup>3+</sup>/Fe<sub>total</sub> is 0.4 for Ryugu and 0.9 for Orgueil). Mg-rich smectite becomes brighter as Fe<sup>3+</sup>/Fe<sub>total</sub> increases from 0.40 to 0.97 (44). The oxidation of phyllosilicates and the formation of epsomite can occur on Earth because of weathering, which we infer is the likely origin of the brightness of Orgueil. Ryugu samples also contain a high abundance of opaque, nano-size pyrrhotite (fig. S10), which acts as a darkening agent; Orgueil lacks these (34), possibly also because of oxidation on Earth (45).

The mineralogy, mineral chemistry, and relative mineral abundances of the major lithology indicate that Ryugu (or its parent body) experienced pervasive aqueous alteration. Except for the lack of sulfate and ferrihydrite, the petrological and mineralogical properties of Ryugu are consistent with the five CI chondrites (31, 32, 34, 46–48); we therefore classified the Ryugu samples as CI chondrites.

### Less altered fragments

Although most Ryugu fragments have experienced extensive aqueous alteration, some fragments in samples of C0002, C0033, C0023, C0025, C0040, C0046, C0076, and C0103 show considerably lesser degrees of alteration. Electron-microprobe analysis (7) indicates that these fragments contain higher abundances of olivine and pyroxene (table S6). Electron diffraction (fig. S17) shows that they also contain calcite or aragonite (not dolomite or breunnerite) and phosphides [schreibersite (Fe, Ni)<sub>3</sub>P and allabogdanite (Fe, Ni)<sub>2</sub>P], not hydroxyapatite. These are characteristic features of a less-altered lithology. These less-altered fragments are enriched in Na, with Na/Si ratios roughly twice that of the Sun (table S7).

We identified five less altered fragments in one of the thin sections of C0002. The Mg map of C0002 (fig. S8B, fragment 1 to 5) indicates a high abundance of olivine and low-Ca pyroxene only in the fragments. These minerals are rich in Mg relative to the surrounding phyllosilicates; we confirmed their presence using an electron microprobe. We also identified spinel



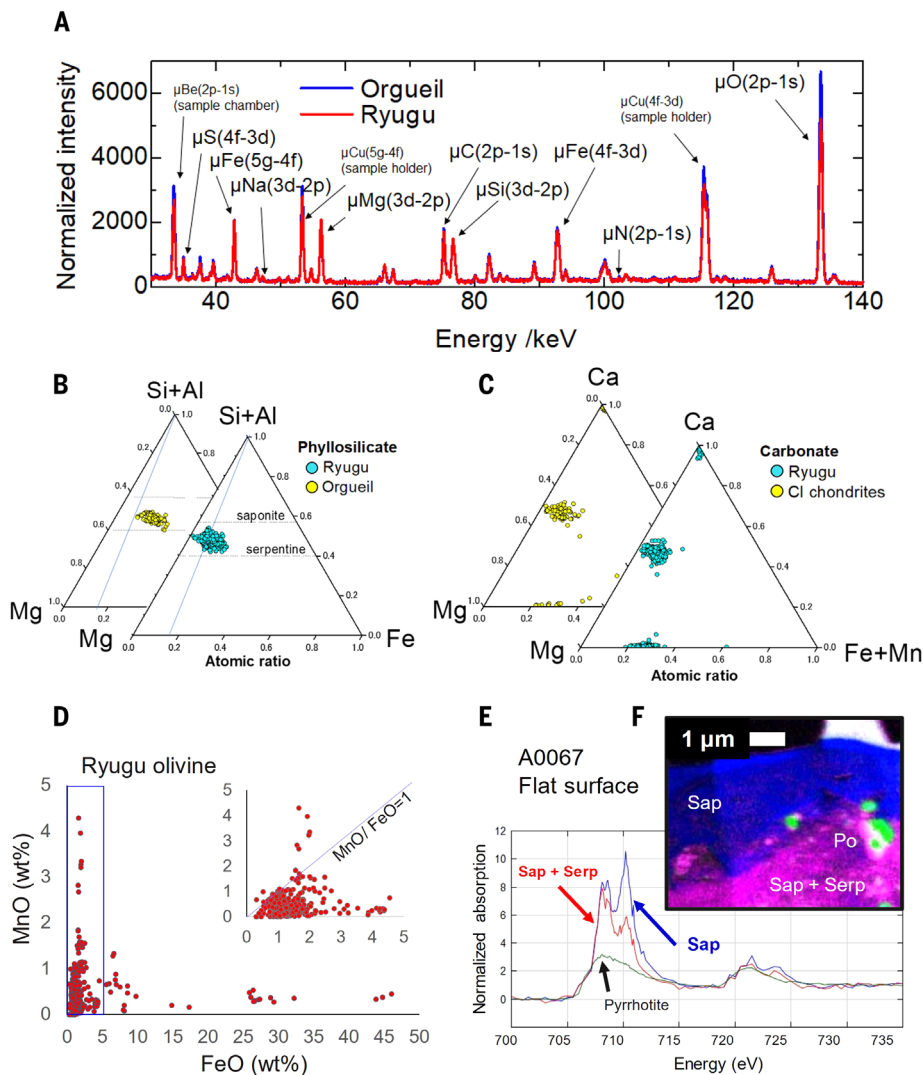


**Fig. 4. Results of chemical analyses using muon, electron, and x-ray spectroscopy.** (A) Muonic x-ray spectra for Ryugu (red) and Orgueil (blue), normalized by means of  $\mu\text{Si}$  3d-2p x-ray (76 keV) intensities (the muonic Si x-ray emitted by transition of 3d to 2p muon atomic orbit). (B) Ternary diagrams of Mg, Fe, and Si+Al, showing the chemical composition of Ryugu phyllosilicates (cyan; 774 analyses), compared with Orgueil (yellow). The blue line corresponds to  $\text{Mg}\# = 85$ . The contribution from FeS was corrected according to S content (7). (C) Ternary diagrams of Mg, Ca, and Fe+Mn showing the chemical composition of Ryugu carbonates (653 analyses), compared with CI chondrites (48, 52). (D) MnO and FeO abundances measured from Ryugu olivine (611 analyses). (Inset) An enlargement of the blue box area in the range from 0 to 5 FeO wt %. The blue line indicates  $\text{MnO}/\text{FeO} = 1$ ; most olivine data have  $\text{MnO}/\text{FeO} < 1$ . (E) XANES spectra [at Fe  $L_{2,3}$ -edge (706.8 eV) and  $L_{3,3}$ -edge (719.9 eV) regions] of a saponite-rich layer (blue), phyllosilicates of the major lithology (red), and pyrrhotite (green). (F) XANES color map of the region shown in Fig. 6B. Three Fe species were identified by means of decomposition analysis (97), including Fe in saponite (blue), in serpentine-saponite (pink), and in pyrrhotite (green).

grains with sizes of  $< 30 \mu\text{m}$  (fig. S18 and table S6). Most olivine in the Ryugu samples occurs in these less altered fragments; the olivine has  $\text{Mg}\# > 97$  (corresponding to  $\text{FeO} < 3 \text{ wt } \%$  in Fig. 4D), which is similar to the olivine in CI chondrites (49–51). A similar, but more altered, fragment has previously been reported in Orgueil [(52), their clast 1].

We identified the two fragments that exhibit the least alteration among our samples,

labeled fragments 4 and 5 in fig. S8B. The fragments are small (130 by  $50 \mu\text{m}$  and 200 by  $90 \mu\text{m}$  for fragments 4 and 5, respectively) (fig. S19) and embedded within the major lithology. They have a very porous texture, dominated by submicrometer particles of olivine, pyroxene, and other smaller silicate phases with numerous iron sulfide inclusions (Fig. 3, D and E). They also contain micrometer-sized Ca carbonate, pyrrhotite, Al spinel, magnetite spher-

ules, small quantities of phosphides, Mg-Na phosphate, pentlandite, chromium (Cr) spinel, and tochilinite [a hydrous sulfide that is abundant in CM2 chondrites (53)] (fig. S20). These mineral assemblages are similar to fragment 1 (fig. S18), but the abundance of olivine and pyroxene is much higher (12.8 and 14.1 vol % for olivine in fragments 4 and 5, respectively) (table S6). Most of the olivine and pyroxene is enriched in Mg, but examples of Fe-rich olivine ( $\text{Mg}\# < 44$ ) are also present. Several small areas in fragment 4 contain Na-rich phyllosilicate, indicating that aqueous alteration fluids were enriched in Na. The high abundance of anhydrous silicates leads us to classify the least altered fragments as CI2 (a CI chondrite that was altered but still retains anhydrous minerals) rather than CII (in which almost all anhydrous silicates are replaced with phyllosilicates).

We observed the least-altered fragments using transmission electron microscopy (TEM) (7) and found that the least-altered fragments also contain numerous partially rounded, mostly 100 to 500 nm, amorphous silicate objects that contain abundant Fe sulfides (mainly  $< 50 \text{ nm}$  pyrrhotite and minor pentlandite) (Fig. 3F and fig. S21A). These objects are similar in texture and composition (fig. S21, A and B) to glass with embedded metal and sulfides (GEMS) that occur in anhydrous chondritic interplanetary dust particles (IDPs) of probable cometary origin (54). The silicates are mostly amorphous or very poorly crystalline material (the latter possibly phyllosilicates), with lattice spacings close to 2.6 and 1.5 Å (fig. S21A). This is similar to fine-grained fibrous material reported in the GEMS-like objects in the Paris CM chondrite (55, 56).

However, there are differences between the least-altered Ryugu fragments and GEMS in IDPs. The GEMS-like objects we identified in Ryugu lack Fe metal, instead containing pyrrhotite, pentlandite, and tochilinite. The silicates have signs of incipient alteration to phyllosilicates (fig. S21A). The Mg-rich silicate composition of the GEMS-like objects in Ryugu is similar to that of the silicates in GEMS in IDPs (fig. S21B) but also to the phyllosilicate composition in the major lithology (Fig. 4B). This indicates that the GEMS-like objects in Ryugu are at least partially altered, which is similar to the primitive clasts in the Paris CM chondrite (55–57).

#### Chondrules, CAIs, and porous olivine

We did not identify any normal-sized chondrules (100 to 1000  $\mu\text{m}$ ) in the Ryugu samples analyzed by using SR-CT. However, some smaller objects and fragments (Fig. 3, G to I) have features characteristic of chondrules. Some of these (Fig. 3, G and H) contain FeNi metal spheres embedded in Mg-rich olivine ( $\text{Mg}\# > 98$ ), which is indicative of melting in very chemically reduced conditions. This is typical of type-I

chondrules, which are defined as those that consist mainly of olivine with  $Mg\# > 90$ . One object has a barred olivine texture in TEM observations (Fig. 3I)—a thin rim and many bars constituting a single crystal of Mg-rich olivine—so we classified this object as a type-I barred olivine chondrule. No glass is present between the olivine bars, only pores, which probably indicates that glass was originally present but dissolved during the early stages of aqueous alteration. We also identified a small ( $\sim 30 \mu\text{m}$  in size) chondrule that has been completely replaced by phyllosilicates (fig. S22 and movie S2). Similar completely altered chondrules have previously been found in the ungrouped C1 chondrite Flensburg, although they are larger ( $> 300 \mu\text{m}$ ) (16). The small sizes and low abundance of the chondrules in Ryugu are similar to those found in samples of the short-period comet 81P/Wild2 (58).

We also identified a few small ( $< 30 \mu\text{m}$ ) CAIs in the Ryugu samples (Fig. 3, K and L). Their sizes are smaller than CAIs in the Ivuna CII chondrite ( $\sim 100 \mu\text{m}$ ) (59). One of the CAIs (Fig. 3K) consists of half hibonite and half Al-rich Fe-free spinel, with a small perovskite inclusion. Another (Fig. 3L) consists of Al-rich Fe-free spinel, with a small hibonite and a perovskite inclusion, and phyllosilicates. We interpreted this as evidence that CAI material that is susceptible to aqueous alteration, such as melilite (60), was replaced with phyllosilicates. Several CAI-related spinel-rich aggregates, together with forsteritic olivine, were also observed (fig. S18).

Forsterite ( $Mg\# 98$  to  $99$ ) grains occur in the less-altered lithology, being  $< 30 \mu\text{m}$  in size with numerous micrometer-size pores. One (Fig. 3J) contains diopside, an Al-, titanium (Ti)-bearing and Ca-, Mg-rich pyroxene. We analyzed 20 grains of porous forsterite by use of an electron microprobe and found that they all contain  $\sim 0.5 \text{ wt } \%$  MnO. Atomic ratios of Mn/Fe do not exceed 1 in most cases, so the grains are not low-iron manganese-enriched (LIME) olivine (67). The pores suggest partial dissolution during aqueous alteration. The origin of this porous olivine is unclear; they could be condensation products, similar to amoeboid olivine aggregates (AOAs) found in carbonaceous chondrites (62), although the texture of the olivine crystals in Ryugu is different from AOAs (63).

### Fluid inclusions in pyrrhotite

We performed higher-resolution ( $\sim 50 \text{ nm}$  per voxel) synchrotron nano-computed tomography (SR-nanoCT) of a large pyrrhotite crystal taken from sample C0002. This crystal showed probable fluid inclusions in the center (Fig. 5, A and B), which suggests that the fluids were trapped in the early stages of crystal growth. These inclusions were completely encapsulated in pyrrhotite and filled with a light-element

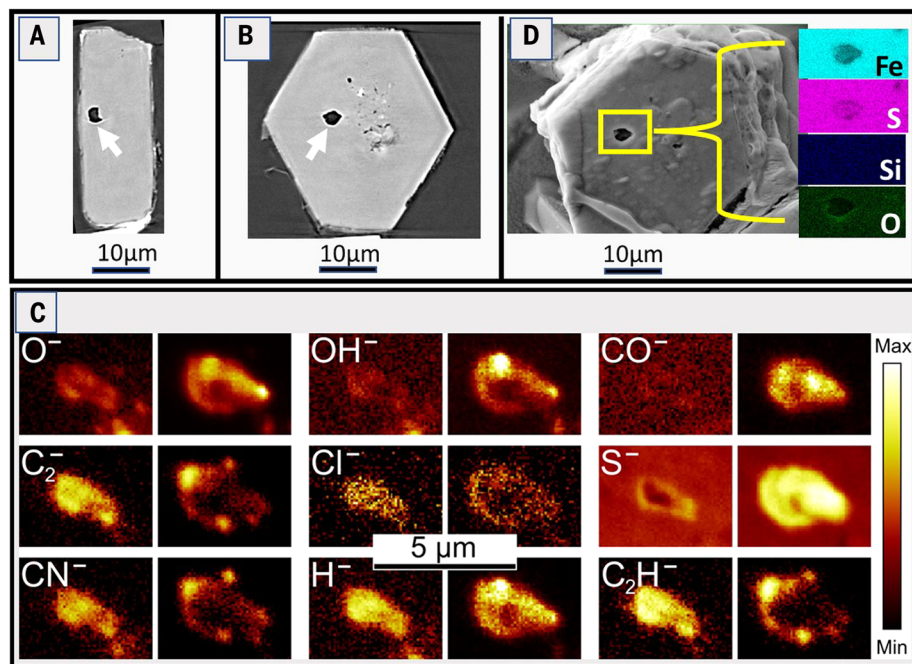


**Fig. 5. A fluid inclusion in a Ryugu pyrrhotite crystal.** TOF-SIMS and SR-nanoCT measurements were performed on a crystal separated from sample C0002. (A and B) Slices through the SR-nanoCT scan, showing that the fluid inclusion (indicated with arrows) is unconnected to the surface, with a minimum depth of  $\sim 1.5 \mu\text{m}$  in (A). (C) TOF-SIMS maps (arbitrary color scale) of the fluid inclusion after being frozen ( $-120^\circ\text{C}$ ) and opened. Representative secondary ion species are labeled on each image pair, which are measured at the top (left images) and the mid-plane (right images) of the fluid inclusion.  $\text{OH}^-$  and  $\text{CO}^-$  are secondary ions of water and  $\text{CO}_2$ , respectively.  $\text{S}^-$  is an ion in the aqueous solution. The presence of  $\text{CN}^-$  indicates N-bearing organic compounds in the fluid, and  $\text{Cl}^-$  indicates that the trapped fluid was a brine. Differences in the distribution of each species within the inclusion, both within each map and between the top and midplane maps, are a result of the distribution of the various fluid components between the different solid phases (solid carbon dioxide, carbon dioxide clathrate, and  $\text{H}_2\text{O}$  ice) that form during cooling of the fluid inclusion to  $-120^\circ\text{C}$ . (D) BSE image of the final surface following the TOF-SIMS measurements, with the opened fluid inclusion in the yellow box. (Insets) Fe, S, Si, and O element maps, measured with EDS, of the region within the box. These indicate that FeS is the host phase.

material (fig. S23). We performed time-of-flight-secondary ion mass spectrometry (TOF-SIMS) depth profiling and lateral mapping ( $< 80 \text{ nm}$  per pixel) at a temperature of  $-120^\circ\text{C}$  to expose and measure, respectively, the composition of the (now frozen) fluids in five inclusions.

The TOF-SIMS measurements show that the trapped fluids were solutions containing  $\text{H}_2\text{O}$ ,  $\text{CO}_2$ , sulfur species, and N- and chlorine (Cl)-bearing organic compounds. These were identified by their representative secondary ion species, including  $\text{O}^-$ ,  $\text{OH}^-$ ,  $\text{CO}^-$ ,  $\text{C}_2^-$ ,  $\text{C}_2\text{H}^-$ ,  $\text{Cl}^-$ ,  $\text{S}^-$ , and  $\text{CN}^-$  (Fig. 5C). The detection of  $\text{CO}^-$ ,  $\text{C}_2^-$ ,  $\text{C}_2\text{H}^-$ , and  $\text{C}_3^-$  indicates that organic molecules were dissolved in the aqueous solution. Electron microscope observations of the largest inclusion show no phyllosilicates or other OH-bearing phases that could have contributed to the signal (Fig. 5D). The presence of  $\text{CO}_2$ -bearing water in a crystal of pyrrhotite indicates that the Ryugu parent body formed beyond the  $\text{CO}_2$  and  $\text{H}_2\text{O}$  snow lines (bounda-

ries between gas and ice in the early Solar System), which were  $> 3$  to  $4$  astronomical units (au) from the Sun (64).

### Flat surfaces and CuS tabular coral-shaped object

We identified some features of the Ryugu samples that have not been observed in meteorites. These include the very flat surfaces of some coarse samples (Fig. 6A). We cut five slices (each  $10$  by  $10$  by  $0.1 \mu\text{m}$ ) from the flat surface of A0067 to perform depth profiles. TEM observations show a  $2\text{-}\mu\text{m}$ -thick saponite-rich layer with high  $Mg\# \sim 90$  running along the flat surface (Fig. 6B). The saponite layer is superposed on an irregular surface of the major lithology, indicating that it formed later. All five slices show similar features, which we infer are present across the whole flat surface. The formation of the saponite layer requires that fluids were present. Pyrrhotite crystals on the flat surface are aligned with their pseudohexagonal facets parallel to the saponite



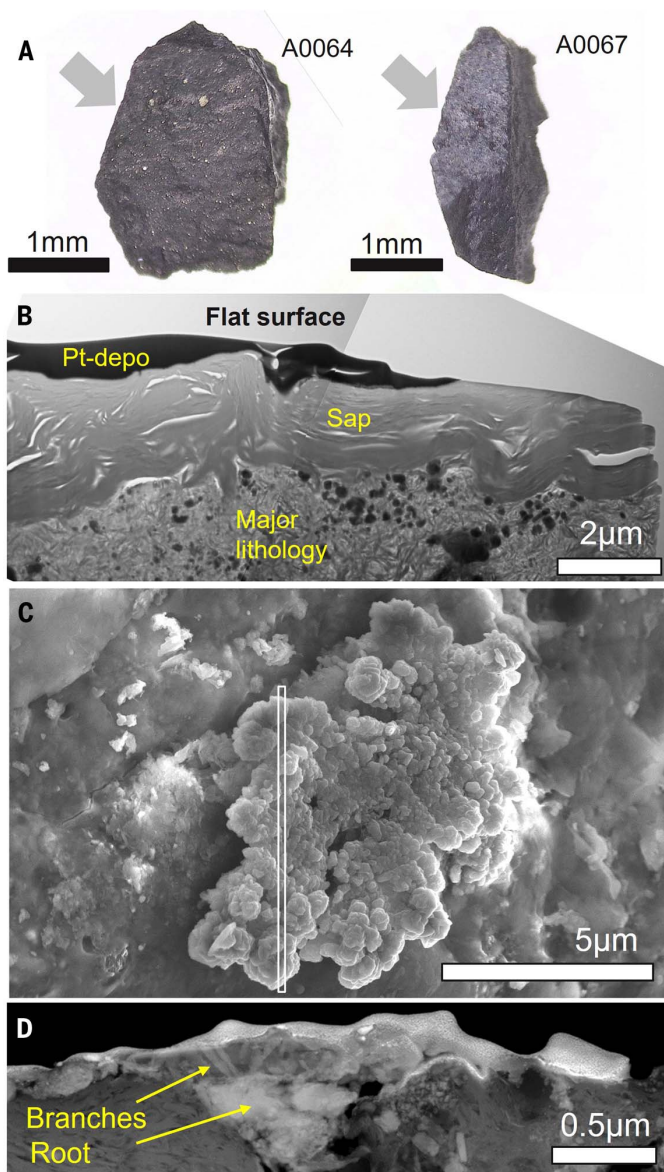


**Fig. 6. Flat surface structures and a CuS table coral-shaped object.** (A) Optical microscope images of flat surfaces (arrows) from two Ryugu samples. (B) Depth profile from a TEM image of a slice cut from the flat surface of A0067 to 5  $\mu\text{m}$  depth. The black layer is contamination from Pt coating. A layer of saponite (interlayer spacing  $d = \sim 10 \text{ \AA}$ ) makes the surface flat. (C) Secondary-electron image of a tabular coral-shaped CuS object on the flat surface of A0067, formed of a stack of submicrometer-sized disk-like crystals. (D) Scanning TEM dark-field image of a slice taken from the white box in (C), perpendicular to the surface to a depth of 10  $\mu\text{m}$  by use of a focused-ion beam. The object has morphologies similar to that of a root, several branches, and a stack of disk-like crystals on top. The thin white layer on the top surface of the object is contamination from a Pt coating.

layer (fig. S24), which implies a compressive force during formation. One possible explanation is ice lensing, the formation and growth of subsurface ice crystals (65, 66), as occurs in permafrost soils. At the final stage of aqueous alteration, fluids could have been segregated in thin cracks as they froze. Ice in the cracks could then have grown to form ice lenses. The pressure exerted by the expanding ice lens could have squeezed the adjacent regolith,

compacting and aligning phyllosilicates, especially expandable clays such as saponite (66).

We also identified table coral-shaped growths of a copper sulfide (CuS) phase on the flat surface of A0067 (Fig. 6C). A thin section was made by cutting the CuS object perpendicular to the flat surface, which was then observed with TEM. The CuS has a morphology that resembles a table coral, with a root, several branches, and many disk-shaped crystals on

top (Fig. 6D). Electron diffraction measurements indicate that the CuS phase is probably digenite ( $\text{Cu}_9\text{S}_5$ ), which is of hydrothermal origin (67). We cannot determine the formation mechanism, but it might have grown from a solution that filled a crack exposed on the flat surface.

#### Shock effects

Most of our samples show no features that indicate strong deformation or shock melting, indicating that the collected material generally did not experience any intense shock. However, C0055 shows evidence of uniaxial compression and sets of parallel fractures perpendicular to the compaction axis (fig. S3). Such features are common in shocked hydrous carbonaceous chondrites (68) and appear in experiments that shocked the Murchison CM2 chondrite to a pressure of 20 GPa (69). Therefore, C0055 experienced a shock, whereas the other 16 samples contain no evidence of shock effects.

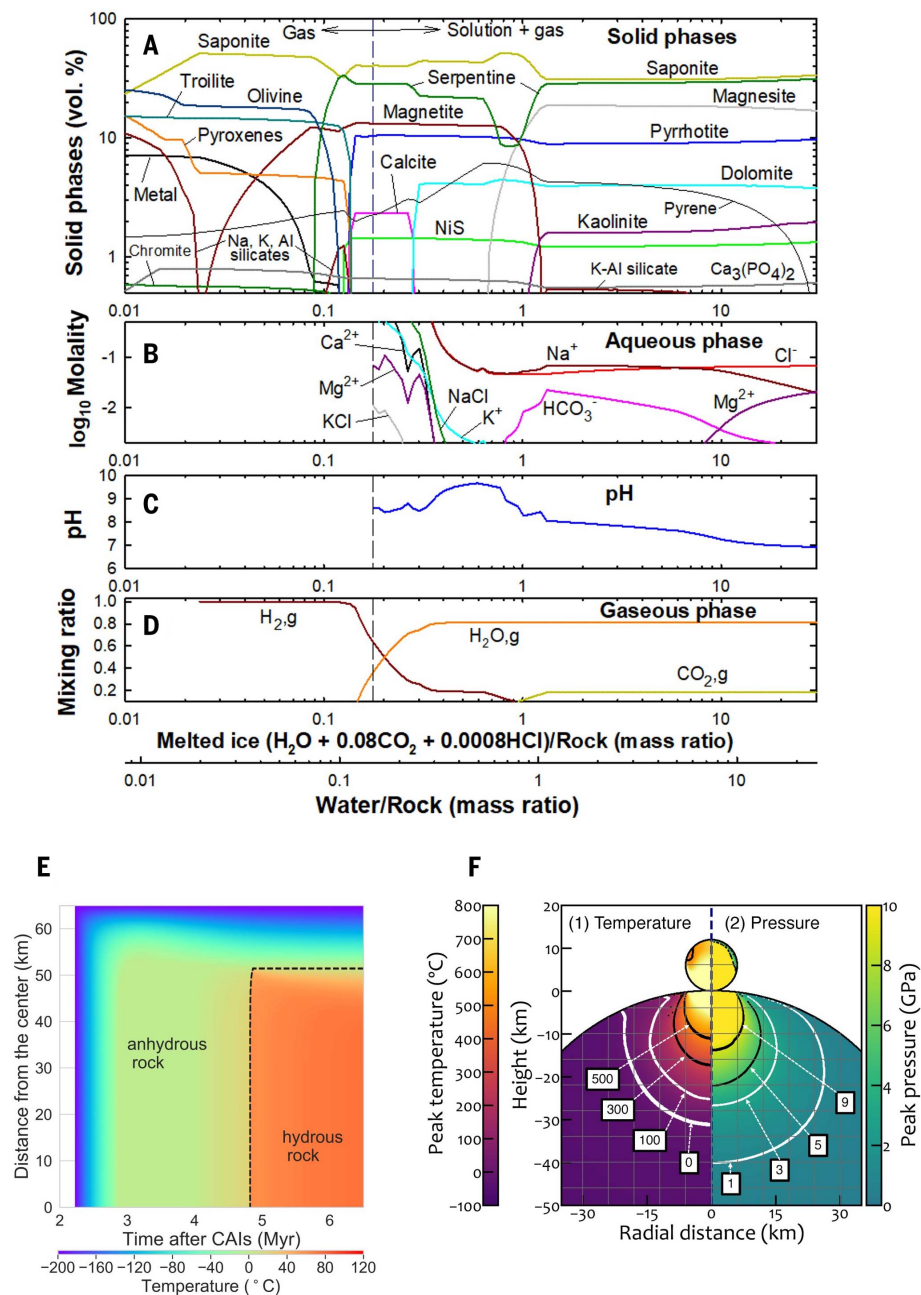
#### Aqueous alteration conditions

The low abundance of Mg-chlorite suggests that aqueous alteration occurred at low temperature, below the  $\sim 100^\circ\text{C}$  (70) required to stabilize Mg-chlorite. All 10 pyrrhotite crystals observed with x-ray and electron diffraction have a monoclinic 4C structure (one of the crystal structures of pyrrhotite, having three unequal crystal axes with one oblique intersection), which indicates that they formed below  $254^\circ\text{C}$  (71). The Ryugu pentlandite and pyrrhotite compositions are most consistent with formation at  $25^\circ\text{C}$  (fig. S25) (67, 72, 73). The site occupancy by Fe and Ni in pentlandite and its lattice constants are a function of temperature (74). We measured the pentlandite lattice constant of  $10.0643 \pm 0.0009 \text{ \AA}$ ; using XRD analysis of a single pentlandite crystal, 5  $\mu\text{m}$  in size, which was separated from sample C0040, following established methods (75). This lattice spacing and the chemical composition indicate an equilibrium temperature of  $20 \pm 29.5^\circ\text{C}$  (table S9). O isotopes in dolomite indicate formation at  $37 \pm 10^\circ\text{C}$  (29). All of these temperature estimates are consistent.

Mössbauer spectra (conventional and synchrotron) were collected from 1-mm-size fragments, taken from C0061 and A0026 under  $\text{N}_2$  gas. These show that magnetite is not oxidized (table S9). The  $\text{Fe}^{2+}/\text{Fe}_{\text{total}}$  ratios measured from the phyllosilicates are approximately 0.61 for C0061 and 0.48 for A0026 (fig. S26). Magnetite, pyrrhotite, and silicates contain 40 to 50%, 15 to 30%, and 25 to 40% total iron, respectively (by atom) (table S9). We performed micro-x-ray fluorescence x-ray absorption near-edge structure ( $\mu\text{-XRF-XANES}$ ) analysis of the Fe K-edge (a sudden increase of x-ray absorption just beyond the binding energy of the K-shell electrons of the Fe atom), using a 1.0-by-1.0- $\mu\text{m}$  x-ray beam (76). Measurements were



**Fig. 7. Calculated models of the aqueous alteration, thermal history, and impact.** (A to D) Model chemical equilibrium of solid, solution, and gas phases during aqueous alteration on the Ryugu parent body at 40°C, assuming the pressure of water saturation ( $7.4 \times 10^{-2}$  bar), and 10% chemically active organic matter. Each line indicates a different species or the pH, as labeled. The vertical dashed lines indicate boundaries between aqueous and water-free conditions. The two horizontal scales indicate ratios of melted ice/rock and  $W/R$ . The ice includes  $\text{CO}_2$  and  $\text{HCl}$  in addition to water, so  $W/R$  is smaller than melted ice/rock by a factor of 0.835. (E) Temperature evolution of the Ryugu parent body. The calculation assumes a 65-km radius with  $W/R = 0.6$  and formation time 2.23 million years after CAI formation. The color scale shows the temperature at each location and time. The black dashed line indicates the boundary between hydrous rock and anhydrous rock, where the highly altered lithology shifts to the less altered lithology. (F) Impact shock model (7), with coordinates measured from the center of the impact point. The images show peak temperature (left) and peak pressure (right) during the impact. The grid of tracer points, placed at multiples of the impactor radius, is shown as gray lines. Isotherms of the peak temperatures are shown as colored curves at 500°, 300°, 100°, and 0°C. Isobaric lines of the peak pressures are shown at 9, 5, 3, and 1 GPa. We infer that the material that later accumulated to form Ryugu was further from the impact than the 100°C isotherm and the 1 GPa isobar.



performed under  $\text{N}_2$  gas, using a 150- $\mu\text{m}$ -size particle separated from sample C0025. They showed that the  $\text{Fe}^{2+}/\text{Fe}_{\text{total}}$  ratio in phyllosilicates is 0.6 to 0.7 (fig. S27), which is consistent with the Mössbauer data.

The determination of  $\text{Fe}^{2+}/\text{Fe}_{\text{total}}$  ratio in other minerals, specifically saponite and serpentine, is required to determine the redox conditions during formation because the stability of  $\text{Fe}^{2+}$  in each phase can be different. We used scanning transmission x-ray microscopy (STXM) (77) analysis with a  $\sim 50\text{-nm}$  spatial resolution to measure  $\text{Fe}^{2+}/\text{Fe}_{\text{total}}$  in the saponite layers in A0067 (Fig. 6B), finding

$0.68 \pm 0.05$  (Fig. 4, E and F). The sample must have been oxidized to some degree during its storage in a desiccator for more than 5 months, so we regard this ratio as a lower limit. On the basis of (i) the relationship between  $\text{Fe}^{2+}/\text{Fe}_{\text{total}}$  ratio and oxidation reduction potential  $E_h$  determined for the minerals nontronite and high-Fe-bearing montmorillonite (78) and (ii) a reduction experiment we performed on terrestrial saponite with  $\text{Fe}^{2+}/\text{Fe}^{3+}$  ratio determined by means of XANES (fig. S28), we infer that the  $\text{Fe}^{2+}/\text{Fe}_{\text{total}}$  ( $> 0.68$ ) obtained from A0067 indicates that the  $E_h$  of saponite formation was likely lower than  $-0.45$  V. If we

assume that this  $E_h$  value is valid at neutral to alkaline pH conditions and combine it with other  $\mu\text{-XRF-XANES}$  data on a dominant oxidized arsenic form ( $\text{As}^{3+}$ ) in As-bearing species in A0067 (fig. S29), we infer fluid  $\text{pH} > \sim 9$  on the basis of the  $E_h$ -pH diagram of As compounds at 25°C (79). The presence of saponite on Ryugu also indicates an alkaline fluid ( $\text{pH} > 8$ ) on the basis of (i) the stability field of saponite in the Eh-pH diagram of Fe and (ii) the pH condition of terrestrial lakes where saponite has been found (80). We conclude that aqueous alteration proceeded at  $\sim 25^\circ\text{C}$  in alkaline conditions.

### Chemical equilibrium modeling of aqueous alteration

Aqueous alteration cannot have begun until accreted ices melted in the interior of Ryugu's parent body and likely continued until temperatures reached  $\sim 40^\circ\text{C}$  [this study and (29)]. We therefore performed chemical equilibrium modeling of a water-gas-solid system at  $0^\circ$  to  $40^\circ\text{C}$  (7). Consistent with the muon analysis (table S3), we assumed the initial accreted rock had the elemental composition of CI chondrites, but with modified amounts of H, C, O, S, and Cl. Our model mixes this rock in different proportions with a water-ice-rich component, which contains  $\text{CO}_2$  and HCl, reflecting the presence of  $\text{CO}_2$  and Cl in the fluid inclusion (Fig. 5) and the inferred C and Cl sources in carbonaceous chondrites (81, 82). Although Ryugu material might not have reached chemical equilibrium during alteration, we ran our calculations to that stage.

Our calculated equilibrium composition of the water-gas-solid system at  $40^\circ\text{C}$  is shown in Fig. 7, A to D, as a function of the initial melted ice/rock and the water/rock ( $W/R$ ) mass ratios. Only 10% of organic matter is allowed to react (7). The modeled mineralogy (Fig. 7A) at initial  $W/R$  of 0.06 to 0.1 reproduces the least-altered lithology we found in the Ryugu samples (table S6). These (and lower)  $W/R$  ratios permit stable reduced phases (such as Fe-rich metal, and phosphides), which could remain unaltered or form through alteration under water-poor and  $\text{H}_2$ -rich conditions. A higher  $W/R$  ratio of 0.1 to 0.2 matches the less-altered lithology, and  $W/R$  of 0.2 to 0.9 with  $\text{pH} > \sim 8.5$  (Fig. 7C) matches with the more extensively altered major lithology (table S6). Analogous calculations were performed at temperatures below  $40^\circ\text{C}$  ( $0^\circ$  and  $20^\circ\text{C}$ ), and the results are similar to those at  $40^\circ\text{C}$  (7).

Our calculations show high Na concentrations at lower  $W/R$ , both in the fluid and in saponite (Fig. 7, A and B), which are consistent with the Na-rich composition of the least- and less-altered lithologies of Ryugu (table S7). The modeling suggests an initial Mg–Na–Cl solution with  $\text{H}_2\text{O}$ – $\text{CO}_2$  in the gas phase, which evolved toward a more reduced and Na–Cl alkaline brine that coexisted with a  $\text{H}_2$ -rich gas phase (Fig. 7, B to D). No sulfates formed in the model because of the reduced conditions, which is consistent with our observations of the Ryugu samples. The formation of sulfates requires strong oxidants—such as  $\text{O}_2$ ,  $\text{H}_2\text{O}_2$ , and  $\text{H}_2\text{SO}_4$ —in ices accreted on asteroids (83).

### Formation of Ryugu's parent asteroid

Ryugu's parent body formed in a different orbit than Ryugu's current near-Earth orbit. Orbital dynamics calculations have shown that the most likely origin of Ryugu is two asteroid families (Eulalia or Polana) in the inner main asteroid belt (3, 4, 84, 85). However, our ob-

servations of  $\text{CO}_2$ -bearing aqueous fluid in Ryugu pyrrhotite is consistent with the parent asteroid having formed beyond the  $\text{H}_2\text{O}$  and  $\text{CO}_2$  snow lines of the early Solar System, more than 3 to 4 au from the Sun. This must have been followed by scattering inward, to the current orbit of the Polana and Eulalia families ( $< 2.5$  au). We found many similarities between the Ryugu samples and CI chondrites, which suggests that CI chondrites might have a similar origin.

The Ryugu samples record a magnetic field (fig. S6), which could have arisen from the nebular magnetic field or the dynamo fields generated by differentiated objects (such as Jupiter), although magnetization effects on Earth are to be corrected. The homogeneous global reflectance spectra of Ryugu indicate that its parent body was not differentiated (2, 3). The stable component of NRM is likely carried by the framboidal magnetite (Fig. 3, A to C). If the source was the nebular field (86), then the solar nebula had not yet dispersed when magnetite formed on Ryugu's parent body.

Our interpretation that Ryugu's parent asteroid formed far from the Sun is supported by (i) the rarity and very small size of chondrules and CAIs in the samples (Fig. 3, G to L), which are similar to those observed in comets (58); (ii) the high abundance of carbonate (table S6); and (iii) the presence of GEMS-like objects (Fig. 3F). However, the C/Si abundance ratio is not as high as those of comets (table S3), according to measurements of cometary IDPs and ultracarbonaceous micrometeorites (30, 87, 88). This indicates that the parent body of Ryugu did not originate from comets themselves but formed in the same region as CI chondrites, at a large heliocentric distance, possibly outside the orbit of Jupiter (89).

### Thermal model of Ryugu's parent asteroid

We used the physical properties obtained from the sample analysis (Table 1) to calculate a thermal model of Ryugu's parent body. The radius of the parent body was chosen on the basis of an estimate of the total mass of the Eulalia family (85). We set a radius of 50 km for the rocky part of the parent body then added additional size according to the amount of water ice in each model. The initial internal and surface temperatures were set to  $-200^\circ\text{C}$  [70 K; rationale provided in (7)]. The temperature was then allowed to increase through heating by radioactive decay of  $^{26}\text{Al}$ , which melted the water ice at  $0^\circ\text{C}$ . Subsequent formation of hydrous minerals (assumed to occur at  $20^\circ\text{C}$ ) released energy that caused further heating. We ran simulations for ranges of formation age ( $t_s$ ) and initial  $W/R$  ratio.

Mn–Cr dating of Ryugu samples has indicated that carbonates formed at  $37 \pm 10^\circ\text{C}$ , 5.2 million years after the formation of the first solid materials in the solar system (CAIs) (29).

That temperature is consistent with our mineralogical constraints (mostly  $\leq 50^\circ\text{C}$ ). Our chemical modeling of the aqueous alteration found that a  $W/R$  ratio of 0.2 to 0.9 reproduces the mineralogy of the major lithology (Fig. 7A). An example thermal model that satisfies these constraints ( $t_s \sim 2.2$  million years and  $W/R = 0.6$ ) is shown in Fig. 7E. Inside the parent body ( $\sim 51$  km radius from the center), the ice melts, hydrous minerals form, and carbonate minerals precipitate at  $\sim 4.8$  million years. Although hydrous and carbonate minerals form throughout, the subsequent temperature increase is limited (reaching a peak of  $\sim 75^\circ\text{C}$ ), and therefore, dehydration of the hydrous minerals does not occur. Within 14 km of the cold surface, ice melting is limited, so the initial mineralogy experiences very little alteration at low  $W/R$  ratios and low temperature ( $\sim 0^\circ\text{C}$ ). Therefore, the least-altered lithology (Fig. 3, D to F) that we found in the Ryugu samples might have been located close to the surface of Ryugu's parent body.

The formation age in the model required to satisfy the constraints from the sample analysis varies depending on the initial  $W/R$ . The major lithology is consistent with  $W/R = 0.2$  to 0.9 (Fig. 7A), which corresponds to a range of formation ages from 1.8 million years ( $W/R = 0.9$ ) to 2.9 million years ( $W/R = 0.2$ ) after CAI formation (conventionally taken to be the beginning of Solar System formation) (fig. S30). We assume instantaneous accretion of the parent body at the time of formation; if the parent body accreted slowly, then the formation must have started earlier.

### Impact on Ryugu's parent body

Ryugu's parent body was disrupted by a large-scale impact to form the Eulalia or Polana asteroid family, including Ryugu itself (3, 90). Using the physical properties measured from the samples (Table 1), we constructed an equation of state consistent with the Ryugu material and used it to calculate a destructive collision with the parent body (7) by use of the impact-simplified arbitrary Lagrangian Eulerian (iSALE) software (91–93). Shown in Fig. 7F is the head-on collision of a 6-km-radius impactor onto a 50-km-radius parent body at an impact speed of  $5 \text{ km s}^{-1}$ , which is typical for the main asteroid belt (94). In this simulation, the parent body is mostly destroyed, with the diameter ( $D$ ) of the largest surviving body being  $\sim 50$  km (fig. S31). This is consistent with the measured sizes of Eulalia ( $D = 40$  km) or Polana ( $D = 55$  km) (85).

Only limited volumes experienced high shock pressure and temperature during the impact (Fig. 7F); we found that 10 and 0.2 vol % of the parent body experienced pressures higher than 1 and 10 GPa, respectively. The temperature near the impact site (approximated as the size of the impactor) rises above  $700^\circ\text{C}$ ,

whereas regions away from the impact site do not rise above 90°C. The latter temperature is consistent with the amount of interlayer water found in Ryugu saponite (29). With this temperature limitation and the absence of evidence for shocks in most of our samples, we propose that Ryugu might have formed from fragments excavated from areas far from the impact site, such as on the far side. It is likely that some of the reaccumulated material originated from the surface and subsurface layer of the parent body; such material would have experienced limited degrees of aqueous alteration at low temperature and low *W/R* ratio, which is consistent with the least-altered and the less-altered fragments found in our samples.

We conclude that the samples collected by the Hayabusa2 mission originated from multiple depths within Ryugu's parent body, which formed beyond the H<sub>2</sub>O and CO<sub>2</sub> snow lines, possibly beyond the orbit of Jupiter.

## REFERENCES AND NOTES

1. S. Watanabe *et al.*, Hayabusa2 arrives at the carbonaceous asteroid 162173 Ryugu-A spinning top-shaped rubble pile. *Science* **364**, 268–272 (2019). doi: [10.1126/science.aav8032](https://doi.org/10.1126/science.aav8032); pmid: [30890588](https://pubmed.ncbi.nlm.nih.gov/30890588/)
2. K. Kitazato *et al.*, The surface composition of asteroid 162173 Ryugu from Hayabusa2 near-infrared spectroscopy. *Science* **364**, 272–275 (2019). doi: [10.1126/science.aav7432](https://doi.org/10.1126/science.aav7432); pmid: [30890589](https://pubmed.ncbi.nlm.nih.gov/30890589/)
3. S. Sugita *et al.*, The geomorphology, color, and thermal properties of Ryugu: Implications for parent-body processes. *Science* **364**, 252 (2019). doi: [10.1126/science.aaw0422](https://doi.org/10.1126/science.aaw0422); pmid: [30890587](https://pubmed.ncbi.nlm.nih.gov/30890587/)
4. E. Tatsumi *et al.*, Spectrally blue hydrated parent body of asteroid (162173) Ryugu. *Nat. Commun.* **12**, 5837 (2021). doi: [10.1038/s41467-021-26071-8](https://doi.org/10.1038/s41467-021-26071-8); pmid: [34611167](https://pubmed.ncbi.nlm.nih.gov/34611167/)
5. E. Tatsumi *et al.*, Collisional history of Ryugu's parent body from bright surface boulders. *Nat. Astron.* **5**, 39–45 (2021). doi: [10.1038/s41550-020-1179-z](https://doi.org/10.1038/s41550-020-1179-z)
6. S. Tachibana *et al.*, Pebbles and sand on asteroid (162173) Ryugu: In situ observation and particles returned to Earth. *Science* **375**, 1011–1016 (2022). doi: [10.1126/science.abe8624](https://doi.org/10.1126/science.abe8624); pmid: [35143255](https://pubmed.ncbi.nlm.nih.gov/35143255/)
7. Materials and methods are available as supplementary materials.
8. F. Vilas, M. J. Gaffey, Phyllosilicate absorption features in main-belt and outer-belt asteroid reflectance spectra. *Science* **246**, 790–792 (1989). doi: [10.1126/science.246.4931.790](https://doi.org/10.1126/science.246.4931.790); pmid: [17748705](https://pubmed.ncbi.nlm.nih.gov/17748705/)
9. P. Beck *et al.*, Hydrous mineralogy of CM and CI chondrites from infrared spectroscopy and their relationship with low albedo asteroids. *Geochim. Cosmochim. Acta* **74**, 4881–4892 (2010). doi: [10.1016/j.gca.2010.05.020](https://doi.org/10.1016/j.gca.2010.05.020)
10. D. Takir *et al.*, Nature and degree of aqueous alteration in CM and CI carbonaceous chondrites. *Meteorit. Planet. Sci.* **48**, 1618–1637 (2013). doi: [10.1111/maps.12171](https://doi.org/10.1111/maps.12171)
11. O. Poch *et al.*, Ammonium salts are a reservoir of nitrogen on a cometary nucleus and possibly on some asteroids. *Science* **367**, eaaw7462 (2020). doi: [10.1126/science.aaw7462](https://doi.org/10.1126/science.aaw7462); pmid: [32165559](https://pubmed.ncbi.nlm.nih.gov/32165559/)
12. T. Morota *et al.*, Sample collection from asteroid (162173) Ryugu by Hayabusa2: Implications for surface evolution. *Science* **368**, 654–659 (2020). doi: [10.1126/science.aaz6306](https://doi.org/10.1126/science.aaz6306); pmid: [32381723](https://pubmed.ncbi.nlm.nih.gov/32381723/)
13. C. Pilorget *et al.*, First compositional analysis of Ryugu samples by the MicrOmega hyperspectral microscope. *Nat. Astron.* **6**, 221–225 (2021). doi: [10.1038/s41550-021-01549-z](https://doi.org/10.1038/s41550-021-01549-z)
14. A. A. Simon *et al.*, Widespread carbon-bearing materials on near-Earth asteroid (101955) Bennu. *Science* **370**, eabc3522 (2020). doi: [10.1126/science.abc3522](https://doi.org/10.1126/science.abc3522); pmid: [33033153](https://pubmed.ncbi.nlm.nih.gov/33033153/)
15. V. E. Hamilton *et al.*, Evidence for limited compositional and particle size variation on asteroid (101955) Bennu from thermal infrared spectroscopy. *Astron. Astrophys.* **650**, A120 (2021). doi: [10.1051/0004-6361/202039728](https://doi.org/10.1051/0004-6361/202039728)
16. A. Bischoff *et al.*, The old, unique CI chondrite Flensburg—insight into the first processes of aqueous alteration, brecciation, and the diversity of water-bearing parent bodies and lithologies. *Geochim. Cosmochim. Acta* **293**, 142–186 (2021). doi: [10.1016/j.gca.2020.10.014](https://doi.org/10.1016/j.gca.2020.10.014)
17. T. Yada *et al.*, Preliminary analysis of the Hayabusa2 samples returned from C-type asteroid Ryugu. *Nature Astron.* **6**, 214–220 (2021). doi: [10.1038/s41550-021-01550-6](https://doi.org/10.1038/s41550-021-01550-6)
18. D. T. Britt, D. Yeomans, K. Housen, G. Consolmagno, "Asteroid density, porosity and structure" in *Asteroids III*, W. F. Bottke, A. Cellino, P. Paolicchi, R. P. Binzel, Eds. (Univ. Arizona Press, 2002), pp. 485–500.
19. C. P. Opeil, D. T. Britt, R. J. Macke, G. J. Consolmagno, The surprising thermal properties of CM carbonaceous chondrites. *Meteorit. Planet. Sci.* **55**, maps.13556 (2020). doi: [10.1111/maps.13556](https://doi.org/10.1111/maps.13556)
20. T. Okada *et al.*, Highly porous nature of a primitive asteroid revealed by thermal imaging. *Nature* **579**, 518–522 (2020). doi: [10.1038/s41586-020-2102-6](https://doi.org/10.1038/s41586-020-2102-6); pmid: [32214245](https://pubmed.ncbi.nlm.nih.gov/32214245/)
21. M. Hamm, I. Pelivan, M. Grott, T. de Wiljes, Thermophysical parameter estimation of small Solar system bodies via data assimilation. *Mon. Not. R. Astron. Soc.* **496**, 2776–2785 (2020). doi: [10.1093/mnras/staa1755](https://doi.org/10.1093/mnras/staa1755)
22. Y. Shimaki *et al.*, Thermophysical modelling and properties of the surface of asteroid 162173 Ryugu: Infrared observations and thermal inertia mapping. *Icarus* **348**, 113835 (2020). doi: [10.1016/j.icarus.2020.113835](https://doi.org/10.1016/j.icarus.2020.113835)
23. S. Sridhar, J. F. Bryson, A. J. King, R. J. Harrison, Constraints on the ice composition of carbonaceous chondrites from their magnetic mineralogy. *Earth Planet. Sci. Lett.* **576**, 117243 (2021). doi: [10.1016/j.epsl.2021.117243](https://doi.org/10.1016/j.epsl.2021.117243)
24. Ö. Özdemir, D. J. Dunlop, Effect of crystal defects and internal stress on the domain structure and magnetic properties of magnetite. *J. Geophys. Res.* **102** (B9), 20211–20224 (1997). doi: [10.1029/97JB01779](https://doi.org/10.1029/97JB01779)
25. K. Shimomura *et al.*, Superconducting muon channel at J-PARC. *Nucl. Instrum. Methods Phys. Res. A* **600**, 192–194 (2009). doi: [10.1016/j.nima.2008.11.029](https://doi.org/10.1016/j.nima.2008.11.029)
26. K. Terada *et al.*, A new X-ray fluorescence spectroscopy for extraterrestrial materials using a muon beam. *Sci. Rep.* **4**, 5072 (2014). doi: [10.1038/srep05072](https://doi.org/10.1038/srep05072); pmid: [24861282](https://pubmed.ncbi.nlm.nih.gov/24861282/)
27. K. Lodders, Relative atomic solar system abundances, mass fractions, and atomic masses of the elements and their isotopes, composition of the solar photosphere, and compositions of the major chondritic meteorite groups. *Space Sci. Rev.* **217**, 44 (2021). doi: [10.1007/s11214-021-00825-8](https://doi.org/10.1007/s11214-021-00825-8)
28. M. Asplund, A. M. Amarsi, N. Grevesse, The chemical make-up of the Sun: A 2020 vision. *Astron. Astrophys.* **653**, A141 (2021). doi: [10.1051/0004-6361/202140445](https://doi.org/10.1051/0004-6361/202140445)
29. T. Yokoyama *et al.*, Samples returned from the asteroid Ryugu are similar to Ivuna-type carbonaceous meteorites. *Science* **379**, eabn7850 (2023).
30. E. Dartois *et al.*, Dome C ultracarbonaceous Antarctic micrometeorites. *Astron. Astrophys.* **609**, A65 (2018). doi: [10.1051/0004-6361/201731322](https://doi.org/10.1051/0004-6361/201731322)
31. J. Alffing, M. Patzek, A. Bischoff, Modal abundances of coarse-grained (>5 μm) components within CI chondrites and their individual clasts – Mixing of various lithologies on the CI parent body(ies). *Chem. Erde* **79**, 125532 (2019). doi: [10.1016/j.chemer.2019.08.004](https://doi.org/10.1016/j.chemer.2019.08.004)
32. A. Morlok *et al.*, Brecciation and chemical heterogeneities of CI chondrites. *Geochim. Cosmochim. Acta* **70**, 5371–5394 (2006). doi: [10.1016/j.gca.2006.08.007](https://doi.org/10.1016/j.gca.2006.08.007)
33. A. J. King, P. F. Schofield, K. T. Howard, S. S. Russell, Modal mineralogy of CI and CI-like chondrites by X-ray diffraction. *Geochim. Cosmochim. Acta* **165**, 148–160 (2015). doi: [10.1016/j.gca.2015.05.038](https://doi.org/10.1016/j.gca.2015.05.038)
34. K. Tomeoka, P. R. Buseck, Matrix mineralogy of the Orgueil CI carbonaceous chondrite. *Geochim. Cosmochim. Acta* **52**, 1627–1640 (1988). doi: [10.1016/0016-7037\(88\)90231-1](https://doi.org/10.1016/0016-7037(88)90231-1)
35. R. G. Burns, D. S. Fisher, Rates of oxidative weathering on the surface of Mars. *J. Geophys. Res.* **98**, 3365–3372 (1993). doi: [10.1029/92JE02055](https://doi.org/10.1029/92JE02055)
36. J. Booth, Q. Hong, R. G. Compton, K. Prout, R. M. Payne, Gypsum overgrowths passivate calcite to acid attack. *J. Colloid Interface Sci.* **192**, 207–214 (1997). doi: [10.1006/jcis.1997.4978](https://doi.org/10.1006/jcis.1997.4978); pmid: [9268560](https://pubmed.ncbi.nlm.nih.gov/9268560/)
37. M. Gounelle, M. E. Zolensky, A terrestrial origin for sulfate veins in CI chondrites. *Meteorit. Planet. Sci.* **36**, 1321–1329 (2001). doi: [10.1111/1945-5100.2001.tb01827.x](https://doi.org/10.1111/1945-5100.2001.tb01827.x)
38. M. Piralla, R. Tartèse, Y. Marrocchi, K. H. Joy, Apatite halogen and hydrogen isotope constraints on the conditions of hydrothermal alteration in carbonaceous chondrites. *Meteorit. Planet. Sci.* **56**, 809–828 (2021). doi: [10.1111/maps.13639](https://doi.org/10.1111/maps.13639)
39. E. De Pauw *et al.*, High energy synchrotron X-ray fluorescence trace element study of a millimeter-sized asteroidal particle in preparation for the Hayabusa2 return sample analyses. *Spectrochim. Acta B At. Spectrosc.* **188**, 106346 (2022). doi: [10.1016/j.sab.2021.106346](https://doi.org/10.1016/j.sab.2021.106346)
40. D. Ward, A. Bischoff, J. Roszjar, J. Berndt, M. J. Whitehouse, Trace element inventory of meteoritic Ca-phosphates. *Am. Mineral.* **102**, 1856–1880 (2017). doi: [10.2138/am-2017-6056](https://doi.org/10.2138/am-2017-6056)
41. M. Endreß, Mineralogische und chemische Untersuchungen an CI Chondriten – Ein Modell zur mineralogisch-kosmochemischen Evolution der(s) CI-Mutterkörper(s), thesis, University of Muenster (1994).
42. P. A. Bland, G. Cressey, O. N. Menzies, Modal mineralogy of carbonaceous chondrites by X-ray diffraction and Mössbauer spectroscopy. *Meteorit. Planet. Sci.* **39**, 3–16 (2004). doi: [10.1111/1945-5100.2004.tb00046.x](https://doi.org/10.1111/1945-5100.2004.tb00046.x)
43. M. N. Bass, Montmorillonite and serpentine in Orgueil meteorite. *Geochim. Cosmochim. Acta* **35**, 139–147 (1971). doi: [10.1016/0016-7037\(71\)90053-6](https://doi.org/10.1016/0016-7037(71)90053-6)
44. S. M. Chembot, R. D. Nickerson, R. V. Morris, D. G. Agresti, J. G. Catalano, Oxidative alteration of ferrous smectites and implications for the redox evolution of early Mars. *J. Geophys. Res. Planets* **122**, 2469–2488 (2017). doi: [10.1002/2017JE005331](https://doi.org/10.1002/2017JE005331); pmid: [32802700](https://pubmed.ncbi.nlm.nih.gov/32802700/)
45. S. Boursiquot, M. Mullet, M. Abdelmoula, J.-M. Génin, J.-J. Ehrhardt, The dry oxidation of tetragonal FeS<sub>1-x</sub> mackinawite. *Phys. Chem. Miner.* **28**, 600–611 (2001). doi: [10.1007/s002690100193](https://doi.org/10.1007/s002690100193)
46. J. F. Kerridge, Major element composition of phyllosilicates in the Orgueil carbonaceous meteorite. *Earth Planet. Sci. Lett.* **29**, 194–200 (1976). doi: [10.1016/0012-821X\(76\)90039-X](https://doi.org/10.1016/0012-821X(76)90039-X)
47. M. E. Zolensky, R. Barrett, L. Browning, Mineralogy and composition of matrix and chondrule rims in carbonaceous chondrites. *Geochim. Cosmochim. Acta* **57**, 3123–3148 (1993). doi: [10.1016/0016-7037\(93\)90298-B](https://doi.org/10.1016/0016-7037(93)90298-B)
48. M. Endreß, A. Bischoff, Carbonates in CI chondrites: Clues to parent body evolution. *Geochim. Cosmochim. Acta* **60**, 489–507 (1996). doi: [10.1016/0016-7037\(95\)00399-1](https://doi.org/10.1016/0016-7037(95)00399-1); pmid: [11539921](https://pubmed.ncbi.nlm.nih.gov/11539921/)
49. A. M. Reid, M. N. Bass, H. Fujita, J. F. Kerridge, K. Fredriksson, Olivine and pyroxene in the Orgueil meteorite. *Geochim. Cosmochim. Acta* **34**, 1253–1255 (1970). doi: [10.1016/0016-7037\(70\)90063-3](https://doi.org/10.1016/0016-7037(70)90063-3)
50. I. M. Steele, Minor elements in forsterites of Orgueil (CI), Alais (CI) and two interplanetary dust particles compared to C2-C3-UOC forsterites. *Meteoritics* **25**, 301–307 (1990). doi: [10.1111/j.1945-5100.1990.tb00714.x](https://doi.org/10.1111/j.1945-5100.1990.tb00714.x)
51. D. R. Frank, M. E. Zolensky, L. Le, Olivine in terminal particles of Stardust aerogel tracks and analogous grains in chondrite matrix. *Geochim. Cosmochim. Acta* **142**, 240–259 (2014). doi: [10.1016/j.gca.2014.05.037](https://doi.org/10.1016/j.gca.2014.05.037)
52. M. R. Lee, K. Nicholson, Ca-carbonate in the Orgueil (CI) carbonaceous chondrite: Mineralogy, microstructure and implications for parent body history. *Earth Planet. Sci. Lett.* **280**, 268–275 (2009). doi: [10.1016/j.epsl.2009.01.038](https://doi.org/10.1016/j.epsl.2009.01.038)
53. I. D. R. Mackinnon, M. E. Zolensky, Proposed structures for poorly characterized phases in C2M carbonaceous chondrite meteorites. *Nature* **309**, 240–242 (1984). doi: [10.1038/309240a0](https://doi.org/10.1038/309240a0)
54. J. P. Bradley, Chemically anomalous, preaccretionally irradiated grains in interplanetary dust from comets. *Science* **265**, 925–929 (1994). doi: [10.1126/science.265.5174.925](https://doi.org/10.1126/science.265.5174.925); pmid: [17782142](https://pubmed.ncbi.nlm.nih.gov/17782142/)
55. H. Leroux, P. Cuvillier, B. Zanda, R. H. Hewins, GEMS-like material in the matrix of the Paris meteorite and the early stages of alteration of CM chondrites. *Geochim. Cosmochim. Acta* **170**, 247–265 (2015). doi: [10.1016/j.gca.2015.09.019](https://doi.org/10.1016/j.gca.2015.09.019)
56. K. K. Ohtaki *et al.*, Search for meteoritic GEMS I: Comparison of amorphous silicates in Paris and Acfer 094 chondrite matrices and in anhydrous chondritic interplanetary dust particles. *Geochim. Cosmochim. Acta* **310**, 320–345 (2021). doi: [10.1016/j.gca.2021.05.042](https://doi.org/10.1016/j.gca.2021.05.042)
57. K. L. Villalon *et al.*, Search for meteoritic GEMS II: Comparison of inclusions in amorphous silicates from the Paris chondrite and from anhydrous chondritic interplanetary dust particles. *Geochim. Cosmochim. Acta* **310**, 346–362 (2021). doi: [10.1016/j.gca.2021.05.041](https://doi.org/10.1016/j.gca.2021.05.041)
58. T. Nakamura *et al.*, Chondrulelike objects in short-period comet 81P/Wild 2. *Science* **321**, 1664–1667 (2008). doi: [10.1126/science.1160995](https://doi.org/10.1126/science.1160995); pmid: [18801994](https://pubmed.ncbi.nlm.nih.gov/18801994/)
59. D. R. Frank *et al.*, A CAI in the Ivuna CI chondrite. *Proceedings of the 42nd Lunar and Planetary Science Conference*, abstract 2785, JSC-CN-22691 (2011).



60. T. J. Fagan, Y. Guan, G. J. MacPherson, Al-Mg isotopic evidence for episodic alteration of Ca-Al-rich inclusions from Allende. *Meteorit. Planet. Sci.* **42**, 1221–1240 (2007). doi: [10.1111/j.1945-5100.2007.tb00570.x](https://doi.org/10.1111/j.1945-5100.2007.tb00570.x)
61. W. Klöck, K. L. Thomas, D. S. McKay, H. Palme, Unusual olivine and pyroxene composition in interplanetary dust and unequilibrated ordinary chondrites. *Nature* **339**, 126–128 (1989). doi: [10.1038/339126a0](https://doi.org/10.1038/339126a0)
62. L. Grossman, I. M. Steele, Amoeboid olivine aggregates in the Allende meteorite. *Geochim. Cosmochim. Acta* **40**, 149–155 (1976). doi: [10.1016/0016-7037\(76\)90172-1](https://doi.org/10.1016/0016-7037(76)90172-1)
63. J. Han, A. J. Brearley, Microstructural evidence for complex formation histories of amoeboid olivine aggregates from the ALHA77307 CO3.0 chondrite. *Meteorit. Planet. Sci.* **50**, 904–925 (2015). doi: [10.1111/maps.12439](https://doi.org/10.1111/maps.12439)
64. A. Tsuchiyama *et al.*, Discovery of primitive CO<sub>2</sub>-bearing fluid in an aqueously altered carbonaceous chondrite. *Sci. Adv.* **7**, eabg9707 (2021). doi: [10.1126/sciadv.abg9707](https://doi.org/10.1126/sciadv.abg9707); pmid: [33883146](https://pubmed.ncbi.nlm.nih.gov/33883146/)
65. M. E. Zolensky, Cyclical regolith processes on hydrous asteroids. *Meteoritics* **30**, 606–607 (1995).
66. L. Zhang, F. Ren, H. Li, D. Cheng, B. Sun, The influence mechanism of freeze-thaw on soil erosion: A review. *Water* **13**, 1010 (2021). doi: [10.3390/w13081010](https://doi.org/10.3390/w13081010)
67. D. J. Vaughan, *Mineral Chemistry of Metal Sulfides* (Cambridge Earth Science Services, 1978). doi: [10.1016/0012-8252\(80\)90122-1](https://doi.org/10.1016/0012-8252(80)90122-1)
68. T. Nakamura *et al.*, Irradiation-energy dependence on the spectral changes of hydrous C-type asteroids based on 4keV and 20keV He exposure experiments of Murchison CM chondrite. *Proceedings of the 51st Lunar and Planetary Science Conference*, abstract 1310 (2020).
69. K. Tomeoka, Y. Yamahana, T. Sekine, Experimental shock metamorphism of the Murchison CM carbonaceous chondrite. *Geochim. Cosmochim. Acta* **63**, 3683–3703 (1999). doi: [10.1016/S0016-7037\(99\)00149-0](https://doi.org/10.1016/S0016-7037(99)00149-0)
70. D. Beaufort *et al.*, Chlorite and chloritization processes through mixed-layer mineral series in low-temperature geological systems—A review. *Clay Miner.* **50**, 497–523 (2015). doi: [10.1180/claymin.2015.050.4.06](https://doi.org/10.1180/claymin.2015.050.4.06)
71. S. A. Kassin, S. D. Scott, Phase relations involving pyrrhotite below 350 degrees C. *Econ. Geol.* **77**, 1739–1754 (1982). doi: [10.2113/gsecongeo.77.7.1739](https://doi.org/10.2113/gsecongeo.77.7.1739)
72. E. L. Berger, D. S. Lauretta, T. J. Zega, L. P. Keller, Heterogeneous histories of Ni-bearing pyrrhotite and pentlandite grains in the CI chondrites Orgueil and Alais. *Meteorit. Planet. Sci.* **51**, 1813–1829 (2016). doi: [10.1111/maps.12721](https://doi.org/10.1111/maps.12721)
73. R. Visser, T. John, M. Patzek, A. Bischoff, M. J. Whitehouse, Sulfur isotope study of sulfides in CI, CM, C<sub>2</sub> and C<sub>3</sub> chondrites and volatile-rich clasts—Evidence for different generations and reservoirs of sulfide formation. *Geochim. Cosmochim. Acta* **261**, 210–223 (2019). doi: [10.1016/j.gca.2019.06.046](https://doi.org/10.1016/j.gca.2019.06.046)
74. K. Tsukimura, H. Nakazawa, T. Endo, O. Fukunaga, Cation distribution in pentlandites (Fe,Ni)<sub>9</sub>S<sub>8</sub>: Dependence on pressure and temperature and kinetics of the cation exchange reaction. *Phys. Chem. Miner.* **19**, 203–212 (1992). doi: [10.1007/BF00202309](https://doi.org/10.1007/BF00202309)
75. K. Sugiyama, T. Kawamata, T. Kuribayashi, Structure refinement of prehnite from Passaic County, New Jersey, USA. *J. Mineral. Petrol. Sci.* **116**, 272–276 (2021). doi: [10.2465/jmps.210318](https://doi.org/10.2465/jmps.210318)
76. H.-B. Qin, Y. Takeichi, H. Nitani, Y. Terada, Y. Takahashi, Tellurium distribution and speciation in contaminated soils from abandoned mine tailings: Comparison with selenium. *Environ. Sci. Technol.* **51**, 6027–6035 (2017). doi: [10.1021/acs.est.7b00955](https://doi.org/10.1021/acs.est.7b00955); pmid: [28426210](https://pubmed.ncbi.nlm.nih.gov/28426210/)
77. Y. Takeichi *et al.*, Design and performance of a compact scanning transmission x-ray microscope at the Photon Factory. *Rev. Sci. Instrum.* **87**, 013704 (2016). doi: [10.1063/1.4940409](https://doi.org/10.1063/1.4940409); pmid: [26827325](https://pubmed.ncbi.nlm.nih.gov/26827325/)
78. C. A. Gorski, L. E. Klüpfel, A. Voegelin, M. Sander, T. B. Hofstetter, Redox properties of structural Fe in clay minerals: 3. Relationships between smectite redox and structural properties. *Environ. Sci. Technol.* **47**, 13477–13485 (2013). doi: [10.1021/es403824x](https://doi.org/10.1021/es403824x); pmid: [24219773](https://pubmed.ncbi.nlm.nih.gov/24219773/)
79. P. Lu, C. Zhu, Arsenic Eh-pH diagrams at 25°C and 1 bar. *Environ. Earth Sci.* **62**, 1673–1683 (2011). doi: [10.1007/s12665-010-0652-x](https://doi.org/10.1007/s12665-010-0652-x)
80. K. Fukushi, Y. Sekine, H. Sakuma, K. Morida, R. Wordsworth, Semiarid climate and hyposaline lake on early Mars inferred from reconstructed water chemistry at Gale. *Nat. Commun.* **10**, 4896 (2019). doi: [10.1038/s41467-019-12871-6](https://doi.org/10.1038/s41467-019-12871-6); pmid: [31653859](https://pubmed.ncbi.nlm.nih.gov/31653859/)
81. C. M. O. D. Alexander, R. Bowden, M. L. Fogel, K. T. Howard, Carbonate abundances and isotopic compositions in chondrites. *Meteorit. Planet. Sci.* **50**, 810–833 (2015). doi: [10.1111/maps.12410](https://doi.org/10.1111/maps.12410)
82. M. Yu. Zolotov, Aqueous fluid composition in CI chondritic materials: Chemical equilibrium assessments in closed systems. *Icarus* **220**, 713–729 (2012). doi: [10.1016/j.icarus.2012.05.036](https://doi.org/10.1016/j.icarus.2012.05.036)
83. M. Yu. Zolotov, Formation of sulfates on parent bodies of carbonaceous chondrites, Ceres, Europa, and other icy bodies. *Proceedings of the 47th Lunar and Planetary Science Conference*, abstract 1778 (2016).
84. H. Campins *et al.*, The origin of asteroid 162173 (1999 JU<sub>3</sub>). *Astron. J.* **146**, 26 (2013). doi: [10.1088/0004-6256/146/2/26](https://doi.org/10.1088/0004-6256/146/2/26)
85. K. J. Walsh, M. Delbó, W. F. Bottke, D. Vokrouhlický, D. S. Lauretta, Introducing the Eulalia and new Polana asteroid families: Re-assessing primitive asteroid families in the inner Main Belt. *Icarus* **225**, 283–297 (2013). doi: [10.1016/j.icarus.2013.03.005](https://doi.org/10.1016/j.icarus.2013.03.005)
86. H. Wang *et al.*, Lifetime of the solar nebula constrained by meteorite paleomagnetism. *Science* **355**, 623–627 (2017). doi: [10.1126/science.aaf5043](https://doi.org/10.1126/science.aaf5043); pmid: [28183977](https://pubmed.ncbi.nlm.nih.gov/28183977/)
87. K. L. Thomas, G. E. Blanford, L. P. Keller, W. Klöck, D. S. McKay, Carbon abundance and silicate mineralogy of anhydrous interplanetary dust particles. *Geochim. Cosmochim. Acta* **57**, 1551–1566 (1993). doi: [10.1016/0016-7037\(93\)90012-L](https://doi.org/10.1016/0016-7037(93)90012-L); pmid: [11539451](https://pubmed.ncbi.nlm.nih.gov/11539451/)
88. M. J. Mumma, S. B. Charnley, The chemical composition of comets—Emerging taxonomies and natal heritage. *Annu. Rev. Astron. Astrophys.* **49**, 471–524 (2011). doi: [10.1146/annurev-astro-081309-130811](https://doi.org/10.1146/annurev-astro-081309-130811)
89. S. J. Desch, A. Kalyaan, C. M. O. D. Alexander, The effect of Jupiter's formation on the distribution of refractory elements and inclusions in meteorites. *Astrophys. J. Suppl. Ser.* **238**, 11 (2018). doi: [10.3847/1538-4365/aad95f](https://doi.org/10.3847/1538-4365/aad95f)
90. P. Michel *et al.*, Collisional formation of top-shaped asteroids and implications for the origins of Ryugu and Bennu. *Nat. Commun.* **11**, 2655 (2020). doi: [10.1038/s41467-020-16433-z](https://doi.org/10.1038/s41467-020-16433-z); pmid: [32461569](https://pubmed.ncbi.nlm.nih.gov/32461569/)
91. A. A. Amsden, H. M. Ruppel, C. W. Hirt, “SALE: a simplified ALE computer program for fluid flow at all speeds,” technical report (Office of Scientific and Technical Information, 1980); doi: [10.2172/5176006](https://doi.org/10.2172/5176006)
92. B. A. Ivanov, D. Deniém, G. Neukum, Implementation of dynamic strength models into 2D hydrocodes: Applications for atmospheric breakup and impact cratering. *Int. J. Impact Eng.* **20**, 411–430 (1997). doi: [10.1016/S0734-743X\(97\)87511-2](https://doi.org/10.1016/S0734-743X(97)87511-2)
93. K. Wünnemann, G. S. Collins, H. J. Melosh, A strain-based porosity model for use in hydrocode simulations of impacts and implications for transient crater growth in porous targets. *Icarus* **180**, 514–527 (2006). doi: [10.1016/j.icarus.2005.10.013](https://doi.org/10.1016/j.icarus.2005.10.013)
94. W. F. Bottke Jr., M. C. Nolan, R. Greenberg, R. A. Kolvoord, Velocity distributions among colliding asteroids. *Icarus* **107**, 255–268 (1994). doi: [10.1006/icar.1994.1021](https://doi.org/10.1006/icar.1994.1021)
95. V. E. Hamilton *et al.*, Evidence for widespread hydrated minerals on asteroid (201955) Bennu. *Nat. Astron.* **3**, 332–340 (2019). doi: [10.1038/s41550-019-0722-z](https://doi.org/10.1038/s41550-019-0722-z); pmid: [31360777](https://pubmed.ncbi.nlm.nih.gov/31360777/)
96. P. Beck *et al.*, Transmission infrared spectra (2–25 μm) of carbonaceous chondrites (CI, CM, CV-CR, C2 ungrouped): Mineralogy, water, and asteroidal processes. *Icarus* **229**, 263–277 (2014). doi: [10.1016/j.icarus.2013.10.019](https://doi.org/10.1016/j.icarus.2013.10.019)
97. I. N. Koprinarov, A. P. Hitchcock, C. T. McCrory, R. F. Childs, Quantitative mapping of structured polymeric systems using singular value decomposition analysis of soft X-ray images. *J. Phys. Chem. B* **106**, 5358–5364 (2002). doi: [10.1021/jp013281l](https://doi.org/10.1021/jp013281l)

## ACKNOWLEDGMENTS

Synchrotron time for XRD and STXM analyses was allocated by the Photon Factory Advisory Committee (proposals 2020S2-002 and 2018S1-001). The SR-CT, SR-nanoCT, and μ-XRF-XANES analyses were conducted under SPRing-8 proposals 2019A-2021A0165, 2019A-2021A0166, 2021B0185, 2021B0188, and 2022A0180. Technical support of the SR experiments at SPRing-8 was provided by RIKEN. The negative muon analysis at MLF, J-PARC was conducted under proposal 2019MS01. Numerical computations for the thermal modeling were carried out on the PC cluster and analysis servers at the Center for Computational Astrophysics of the National Astronomical Observatory of Japan. We thank the developers of iSALE, including G. Collins, K. Wünnemann, B. Ivanov, J. Melosh, D. Elbeshausen, and T. Davison. We acknowledge the ESRF for provision of beamtime at beamline ID15A (proposal ES-1017). This research used resources of the Advanced Photon Source, a US Department of Energy (DOE) Office of Science User Facility at Argonne National Laboratory. We thank A. Simon and V. Hamilton for providing the spectra of asteroid Bennu, and Toyo Corporation for the use of the pFIB system for sample

preparation. We also thank many researchers who have contributed to the various experiments and measurements, especially H. Nakao, R. Watanabe, S. Kobayashi, K. Mogi, Y. Kousaka, E. Tomosada, T. Morita, M. Nakamura, O. Sasaki, K. Saito, T. Konno, T. Miyazaki, Y. Ito, K. Onodera, S. Hasegawa, G. Nishikawa, T. Kobayashi, S. Murakoshi, K. Goto, Y. Tanaka, K. Hattori, M. Yoshioka, K. Tomioka, T. Kawahara, S. Tachikawa, T. Nishi, H. Ohta, M. Suga, T. Sunagawa, O. Nishizawa, K. Kitamura, K. Sawayama, T. Hatakeyama, S. Steve, S. Sutton, R. Jones, R. Yoshida, H. Kasai, T. Akashi, I. Hitachi, A. Dazzi, A. Deniset-Besseau, L. Bejach, J. Garrevoat, M. Michiel, T. Azuma, K. Mizumoto, T. Minami, K. Shimomura, S. Takeda, M. Katsuragawa, A. Yamaguchi, T. Yomogida, D. Wakabayashi, S. Lefrançois, E. Heripré, D. Troadec, J. Garrevoat, M. di Michiel, O. Mivumbi, C. Sandt, Z. Rahman, L. Le, F. Capitani, and Shimizu Corporation for their technical support. **Funding:** This work was supported by KAKENHI from the Japanese Society for Promotion of Science (JSPS); grants JP20H00188 and 19H05183 to T.Na.; JP19K14776 to M.Matsum.; 21K18645 to T.Mik. and K.Sugiy.; JP20H0205 to A.Ts., M.Matsum., A.Miyak., and J.Mats.; 17H06458 to K.F., Y.Taka., S.Yamas., and M.Kim.; JP17H06459 to T.Na., T.U., S.Wat., M.Matsuo., N.N., T.Mo., T.Ok., Y.S., N.S., and R.N.; JP15H05695 to A.Ts. and K.U.; 20H05846 to S.Tac.; JP17H06457 to H.G.; JP19H00726 to K.Kur., H. G., and T.Mik.; JP21J13337 to K.A.; JP18H05456 and JP20H00189 to K.Sugiy.; 18H05463 to T.Tak., S.Nakas., and S.Wat.; 18H05460 to K.Nin. and T.Os.; 18H05464 to Y.Miy.; 18H05457 to K.Nin., T.Tak., S.Wat., and Y.Miy.; and JP18H05479 to M.U. This work was also supported by the JSPS Core-to-Core program “International Network of Planetary Sciences” and the Ministry of Education, Culture, Sports, Science and Technology (MEXT) (grants JPMXS0450200421 and JPMXS0450200521 to S.S.); A.J.K. acknowledges funding support from UK Research and Innovation (UKRI) grant MR/T020261/1. A.J.B. acknowledges funding support from NASA Emerging Worlds grant 80NSSC18K0731. P.B. acknowledges funding from the European Research Council (ERC) under grant agreement 771691 (Solarys) and the CNES, R.B. and F.B. acknowledge support by Region Ile-de-France (DIM-ACAV) and SOLEIL for the FTIR micro-spectroscopy measurements. F.E.B. and B.J.T. acknowledge funding from German Research Foundation DFG grant BR2015/38-1 and Dr. Ralph Schwieter Foundation. L.V. and B.B. acknowledge support from Ghent University Special Research Fund Grants BOF-OIGC1517 and Research Foundation Flanders grants GD55221N and 1205322N. B.V. acknowledges funding from BOF17-GO-015. P.T. acknowledges funding from Ghent University Special Research Fund Grants BOF20/PDO/037 and Research Foundation Flanders grants GD55221N and 1205322N. M.R. acknowledges the French PICS-CNRS funding program, the French ANR (CLASSY) and the FACCTS program, and funding from the DOE Office of Science Basic Energy Sciences, under contract DE-AC02-06CH11357. M.R. and J.C.V. benefited from the Ile de France DIM ACAV+ funding (PARYUGU). M.Y.Z. is supported by NASA grants 80NSSC19K0786 and 80NSSC19K0313. A.Ts. is supported by Chinese Academy of Sciences President's International Fellowship Initiative, grant 2019VCA0004. D.L.D. is supported by NASA grants NNX16AL34G and 80ARCO17M00005. E.P. acknowledges funding from Italian Space Agency (ASI) through contract 2018-27-HH-O. F.V., A.R.H., and C.J. acknowledge funding from NASA's TREC note of the Solar System Exploration Research Virtual Institute 2016 (SSERVI16) Cooperative Agreement (NNH16ZDA00IN). G.D. acknowledges NASA LARS funding of NanoIR technique development (80NSSC19K1051). M.E.Z. is supported by NASA Hayabusa2 Mission Participating Scientist Program. M.Tan. is supported by JSPS KAKENHI grant 21K03654. C.E., J.D., E.Da., and J.Math. acknowledge funding from CNES (MIAMI2), DIM-ACAV+ (C3E), LabEx P2IO, and ANR (COMETOR ANR-18-CE31-0011). R.B., A.Alé., Z.Di., C.L., Z.Dj., D.Ba., L.R., S.R., and C.P. acknowledge support by the CNES. K.A. is supported an GP-EES Research Grant. Z.G. acknowledges the Molecular Foundry, supported by the Office of Science, Office of Basic Energy Sciences, of the U.S. Department of Energy under Contract No. DE-AC02-05CH11231. **Author contributions:** Organizing the research, writing the manuscript, main sample analysis: T.Na. Writing the manuscript, main sample analysis: M.Matsum., Y.E., K.A., and M.E.Z. Electron microscopy: M.Matsum., Y.E., M.E.Z., T.Mik., D.N., M.Kik., A.J.B., Y.K., D.Br., D.J.J., J.Mar., J.H., H.Yo., A.N., T.No., C.E., J.D., S.S.R., C.M., T.Tan., K.Ts., S.Yamad., K.Ya., S.A., Y.A., S.D.S., T.F., T.Kat.F.L., T.Ma., H.M., and A.Miyak. Synchrotron experiments: Y.Tak., Y.F., A.Ts., M.U., J.Mats., M.Tak., F.E.B., B.J.T., L.V., M.R., J.-C.V., P.B., E.E.A., M.Tan., K.F., H.Su., S.Yamas., T.Kawai., K.I., E.B., S.E., P.T., Y.Takeic., A.Take., A.Taki., M.Yas., K.U., S.O., O.S., M.Su., E.Da., E.De., Z.Di., Z.Dj., G.Kif., K.Hag., M.Y.H., M.Kim., B.L., M.L., J.Z., B.V., D.Ba., B.B., F.B., K.Nit., J.Math., I.M., R.B., A.Alé., C.M., and J.D.

S.R. Muon analysis: K.Nin., T.Tak., T.Os., K.Te., T.W., S.Wat., S.Tak., A.Tan., I.U., I.C., M.K.K., S.Nag., and Y.Miy. Physical property measurements: S.Tan., H.Nag., M.Sa., T.Mic., Y.N., T.Ts., Y.In., R.E., T.Yag., T.Is., A.Ala., N.S., R.Fuj., T.Kawamu, and Y.Yamas. Numerical simulations: H.G., M.Y.Z., K.Kur., S.Wak., and R.Hy. Reflectance spectra: K.A., E.K., M.Matsuo, R.E.M., E.T., S.S., T.Hi., K.Ki., Q.H.S.C., F.V., A.R.H., C.J., D.L.D., G.D., Z.G., T.Kawamo., L.R., S.R., D.T., Y.Yamas., E.P., C.P., S.M.P., C.S., C.L., R.B., A.Alé., K.Sugiu., and G.N. TOF SIMS analysis: A.D., R.J.B., and I.R.G. XRD analysis: K.Sugiy., and A.J.K. Interdiscipline science discussion: H.Yu., R.O., H.Yab., H.Nar., K.Sa., S.Tac., H.C.C., and D.S.L. Hayabusa2 mission sample collection: M.Yoshit., M.Yoshik., K.Yoshik., K.Yoshih., Y.Yo., K.Yo., H.Ya., Y.Yamam., D.Y., M.Yam., T.Yam., T.Yad., K.W., T.U., R.T., F.T., H.T., Y.Takei., A.I., H.So., K.Sh., Y.S., H.Se., H.Sa., T.S., M.O., G.O., T.Ok., N.O., K.O., R.N., H.No., M.N., N.N., S.Nak., T.Mo., A.Miyaz., A.Miu., Y.Mim., K.M., K.Kum., T.Ko., S.Ki., K.Ka., S.Ka., T.Iw., Y.Is., M.I., H.I., S.H., R.Ho.,

C.H., Y.H., Nar.H., Nao.H., T.Ha., M.H., K.Hat., S.F., R.Fuk., A.F., Y.C., M.Ar., M.Ab., S.Wat., and Y.Ts. All authors discussed the results and commented on the manuscript. **Competing interests:** We declare no competing interests. **Data and materials availability:** All images and raw data used in this study are available at the JAXA Data Archives and Transmission System (DARTS) at [https://data.darts.isas.jaxa.jp/pub/hayabusa2/paper/sample/Nakamura\\_2022](https://data.darts.isas.jaxa.jp/pub/hayabusa2/paper/sample/Nakamura_2022). Software code, scripts, and input files for the thermal modeling, chemical modeling, and impact simulations are also available at the same URL. Other data on the Ryugu sample and from the Hayabusa2 mission are available at the DARTS archive at <https://www.darts.isas.jaxa.jp/curation/hayabusa2> and <https://www.darts.isas.jaxa.jp/planet/project/hayabusa2>, respectively. The returned samples are curated by JAXA Astromaterials Science Research Group, who distribute them through an Announcement of Opportunity available at <https://jaxa-ryugu-sample-ao.net>. **License information:** Copyright © 2023 the authors, some rights

reserved; exclusive licensee American Association for the Advancement of Science. No claim to original US government works. <https://www.science.org/about/science-licenses-journal-article-reuse>

#### SUPPLEMENTARY MATERIALS

[science.org/doi/10.1126/science.abn8671](https://doi.org/10.1126/science.abn8671)

Materials and Methods

Supplementary Text

Figs. S1 to S47

Tables S1 to S15

References (98–189)

Movies S1 and S2

Submitted 25 December 2021; accepted 5 September 2022

Published online 22 September 2022

10.1126/science.abn8671